2014-10-10

Development of tissue directionality-based measures of demyelination and remyelination for multiple sclerosis using structure tensor analysis

Kamalpour-Ansari, Mohammad hadi

UNIVERSITY OF CALGARY

DEVELOPMENT OF TISSUE DIRECTIONALITY-BASED MEASURES OF DEMYELINATION AND REMYELINATION FOR MULTIPLE SCLEROSIS USING STRUCTURE TENSOR ANALYSIS

by

MOHAMMAD HADI KAMALPOUR-ANSARI

A THESIS

SUBMITTED TO THE FACULTY OF GRADUATE STUDIES

IN PARTIAL FULFILMENT OF THE REQUIREMENTS FOR THE

DEGREE OF MASTER OF SCIENCE

GRADUATE PROGRAM IN NEUROSCIENCE

CALGARY, ALBERTA

AUGUST, 2014

Abstract

Changes in myelin integrity are key characteristics of many diseases including multiple sclerosis. The goal of this project was to evaluate the feasibility of structure tensor analysis, a potentially new measure of tissue directionality, to measure myelin health. Using histology and MR images obtained from a lysolecithin model of demyelination and remyelination, I quantified the coherency (anisotropy), energy (organization), and entropy (heterogeneity) of white matter in mouse spinal cords with different myelin integrity and found that demyelinated tissue had lower coherency and energy but higher entropy than tissues with intact myelin. I also tested the robustness of this technique to the change in image size in MRI and showed its practical feasibility. My findings suggest that tissues with better myelin integrity have greater alignment and anisotropy. Structure tensor analysis may have the potential to evaluate de- and re-myelination in patients with multiple sclerosis and similar disorders. Further validation is warranted.

Acknowledgements

First and foremost, I would like to give thanks and praise to the Almighty God for His grace and blessings throughout my life. I could have never been to where I am today without the faith I have in Him. I would like to express my sincere thanks and appreciation to my supervisor Dr. Yunyan Zhang for her invaluable support, guidance, and encouragement throughout my Masters. I am deeply grateful for her excellent mentorship and exceptional supervision of my work. I am sincerely grateful to my co-supervisor Dr. V Wee Yong for his advice, professional expertise and continuous enthusiasm.

I express my warmest appreciation to my supervisory committee, Dr. Jeff Dunn and Dr. Luanne Metz for their guidance, continuous support and mentorship throughout my Masters. I also wish to express my sincere thanks to my external examiner Dr. Bruce Pike for assessing my thesis.

I am deeply indebted to my parents who guided me to where I am today. I am forever grateful for their continuous encouragement, patience, understanding and invaluable support.

Finally, I would like to thank Alberta endMS research and training network for the training opportunity.

Dedication

To my inspiriting parents and sister, Abolfazl, Nahid and Fatemeh for their unwavering support and encouragement over the years.

Table of Contents

List of Tables

List of Figures

List of Symbols, Abbreviations and Nomenclature

Symbol	Definition
MS	Multiple Sclerosis
CNS	Central Nervous System
MRI	Magnetic Resonance Imaging
LFB	Luxol Fast Blue
OPC	Oligodendrocyte Precursor Cells
LPC	Lysophosphatidyl Choline
Gd-DTPA	Gadolinium Diethylenetriamine
MTR	Magnetization Transfer Ratio
MWF	Myelin-Water Fraction
NAWM	Normal Appearing White Matter
DTI	Diffusion Tensor Imaging
FA	Fractional Anisotropy
MD	Mean Diffusivity
FT	Fourier Transform
2D	2 Dimensional
ROI	Region Of Interest
ANOVA	Analysis Of Variance
EAE	Experimental Autoimmune Encephalomyelitis
B-spline	Basis Spline

Epigraph

What is essential is invisible to the eye.

—The Little Prince, Antoine De Saint-Exupéry, 1943

Chapter One: **Introduction**

1.1 Overview of Research

Multiple sclerosis (MS) is a severe demyelinating disease of the central nervous system (CNS) that primarily affects young adults. Approximately 2 million people are impacted worldwide, including 100,000 unfortunate Canadians (1, 2). Within 10-15 years of disease diagnosis, over 20% of people with MS require the aid of a wheel chair, with significant loss of neurological function and quality of life (3); presently, there is no cure for MS. Pathologically, MS is characterized by multi-focal plaques, reflecting variable degrees of tissue injury (4). Currently, as an important repair strategy, remyelination is also shown to occur in MS lesions following demyelination although it is not sufficient in most and fails in many patients (5). Therefore, accurate measurement of de- and re-myelination in MS lesions may improve our understanding of disease evolution and help discover novel medicines for MS patients.

There has been an ongoing challenge in measuring de- and re-myelination in MS. In histopathology, myelin content can be detected using dedicated stains, but few histological findings are directly translatable to magnetic resonance imaging (MRI). In clinical studies, conventional MR imaging is routinely used for MS diagnosis and for assessing lesion activity in MS patients (6); however, conventional MRI is not specific to the pathological changes of the disease. Thus, there is a clear need for specific measures of de- and re-myelination, ideally applicable in the clinical setting. In this thesis, my aim was to investigate the feasibility and potential of a new quantitative imaging method, which estimates the directionality of tissue structure, to assess de- and re-myelination in an animal model; I also aim to test the utility of this method in conventional MR imaging.

1.2 Impact of De- and Re-myelination on Tissue Orientation

The myelin sheath is a highly organized structure that protects the underlying axons from damage while enhancing the conduction velocity of nerve impulses. The uniform alignment of these myelin sheaths is associated with the anisotropic orientation of myelinated nerve fibers (7). Upon demyelination, this oriented structure is disrupted. Depending on the extent of myelin damage following demyelination, the alignment and anisotropy of nerve fibers is altered (8). Simultaneously after demyelination, a large amount of myelin debris is created in the vicinity of the injury site. Although these components are dynamically cleared prior to remyelination, myelin fragments may impact the degree of tissue anisotropy and complicate the measurement, particularly using MRI in vivo. Remyelination can help restore the lost anisotropy of nerve fibers by generating new myelin sheaths, but they are thinner and shorter between nodes than those in normal myelin (9). Partially recovered myelin structure in remyelinated lesions should be different from healthy myelin and from fully demyelinated lesions in the alignment and anisotropy, and this difference may be distinguished using quantitative analysis.

1.3 Thesis Overview

In this thesis, I adapted a directionality-based technique named structure tensor analysis to quantify the alignment and integrity of nerve fibers in white matter lesions with different degrees of myelination. Using a mouse model, I tested the validity of this method in histological images and its utility to assess de- and re-myelination in standard MR images. Based on mathematical calculation, several tissue orientation-related indices can be extracted. In this project, I studied the coherency and energy of tissue structure and derived an outcome named angular entropy based on the directional distribution in a tissue. Coherency quantifies the degree of tissue

alignment; energy evaluates the directional organization of tissue pathology, and angular entropy measures the heterogeneity of a tissue.

Structure tensor analysis has been used to assess the directional property of tissue structure in different organs, mostly in animal models but rarely in the central nervous system (10, 11). Recently, structure tensor analysis has been applied to evaluate the orientation of human corpus callosum nerve fibers (12). So far, the applications of structure tensor analysis have been based on histological images to study overall tissue orientation, where myelin-related directionality has not been explored. It is believed that changes in myelin content could be followed by myelin-specific staining of histological images (13). The change in myelin integrity alters the underlying pathology, which may be shown through the pixel intensity-related changes in MR images upon de- and re-myelination (14). Therefore, the focus of this thesis is to use structure tensor analysis to assess myelin-related tissue alignment in de- and re-myelination in histology and MRI.

1.3.1 Hypothesis and Statement of Aims

Demyelination and remyelination are important features of MS lesions; however, their in vivo detection and measurement using MRI has been challenging. Given the fact that demyelination disrupts the anisotropic features of tissue structure while remyelination partially restores these properties, the content and organization of tissue structure may be detected based on the alignment of oriented structures. In this thesis, I tested the *hypothesis that tissue directional property changes with demyelination and remyelination and that these changes can be identified using structure tensor-based outcome measures*. My overall goal was to develop an imaging outcome of de-and re-myelination based on structure tensor analysis. I examined both

histological and T_2-weighted MR images derived from a lysolecithin model of demyelination, followed by spontaneous remyelination in mouse spinal cords. My specific aims were:

Aim 1: To validate the ability of structure tensor analysis to discriminate myelinated and demyelinated tissue types using histological images.

Aim 2: To assess the robustness of structure tensor outcomes to different interpolation methods and image resolutions commonly used in MR imaging.

Aim 3: To evaluate the feasibility of using structure tensor measures to evaluate demyelination and remyelination in the standard MRI of lysolecithin mice, acquired from a high-field animal scanner in vivo.

1.4 Thesis Organization

Chapter one outlines the research overview, hypothesis and goals studied in this thesis. Chapter two describes the disease MS, its pathology and potential measurement tools using MRI, particularly regarding de- and re-myelination. This is followed by a systemic review of several MR imaging techniques that are myelin-relevant. Specifically, I described the acquisition and application of conventional MRI, magnetization transfer imaging, myelin-water imaging, diffusion tensor imaging and susceptibility based-MRI and the theory and utility of multiple image processing-based methods that have the potential to assess tissue directionality or integrity, which include Fourier distribution analysis, image texture analysis and structure tensor analysis. From chapter three to chapter five, the evaluation of structure tensor-based outcome

measures in standard images is discussed. Specifically, Chapter three illustrates the ability of structure tensor analysis to distinguish healthy (non-demyelinated), lesion (demyelinated) and border (partially demyelinated) tissues as shown in myelin-stained histological images. These images were obtained from the spinal cord of the mouse model. Chapter four describes the feasibility of using structure tensor analysis in conventional MR images. This is tested in images with different matrix size, which are achieved by using three different interpolation methods. Both the robustness of structure tensor-based measures to each interpolation method and the reliability of interpolation techniques are investigated. Chapter five describes the utility of structure tensor analysis for assessing de- and re-myelination in T_2-weighted MRI acquired in vivo. Using the same mouse model described in Chapter three, demyelinated lesions were generated in the dorsal column of mouse spinal cords. The periods of de- and re-myelination were non-invasively followed by MRI at 9.4 Tesla for up to 35 days when evident remyelination was expected. I applied the same strategy to assess changes in directional metrics at day 0 (normal myelin), day 7 (demyelinated lesion), and days 28-35 (remyelinated lesion). Finally, Chapter six summarizes the findings of this project, discusses future directions, and highlights the importance of this work to people with MS and other demyelinating diseases.

Chapter Two: **Background and Literature Review**

2.1 Overview of MS

MS is a complex and severe inflammatory demyelinating disorder affecting the CNS. It is more prevalent in North American and European countries that are further way from the equator and that experience temperate climates (15, 16). The prevalence of MS is at least two times higher in females than in males, mostly between 20 to 40 years old (17). Most of the patients start with a relapsing-remitting disease course, which over time develops as secondary progressive MS, but some experience steady progression from the beginning of the disease, called primary progressive MS (18). Progression of MS leads to significant cognitive, sensory, motor and autonomic deficits in MS patients, presenting with symptoms such as vision impairment, muscle weakness, depression, and painful spasms (19). While mechanisms are not fully understood, multi-focal lesions in the brain and spinal cords are believed to play a major role in the progression of patient disability (20). In each lesion, several pathological processes can be found including inflammation, edema, axonal damage, gliosis, and the key manifestations of MS: demyelination and remyelination.

2.2 Demyelination and Remyelination in Multiple Sclerosis

Demyelination is the process damaging the protective myelin sheath and the myelin-forming oligodendrocytes (21, 22). In MS, demyelination can be caused by inflammatory processes and is associated with neuronal and nerve injury subsequently (16, 23). Demyelination can occur anywhere in the brain and spinal cords of MS patients but white matter tracts are typically affected (24). The breakdown of myelin leads to decreased conduction of nerve impulses along axons that are associated with a variety of neurological symptoms (25). Demyelination can be

evaluated by a variety of staining methods in histology sections, such as those using luxol fast blue (LFB) and eriochrome cyanine R.

Following demyelination, the process of remyelination may occur in some MS patients, especially in acute MS lesions (figure 2.1) (26). Remyelination is the repair of myelin sheath by mature oligodendrocytes (figure 2.2). After demyelination, oligodendrocyte precursor cells (OPC) migrate to the lesion site and differentiate into mature oligodendrocytes that give rise to functional myelin sheaths (5). Prior to this, the infiltration of macrophages to the lesion site is required to eliminate myelin debris for optimal OPC survival (27, 28). Remyelinated lesions appear as shadow plaques in histology sections (29) and can be measured through g-ratio calculations (30). The g-ratio refers to the ratio of axonal circumference to myelinated fiber circumference, where a smaller ratio corresponds to higher degree of myelination.

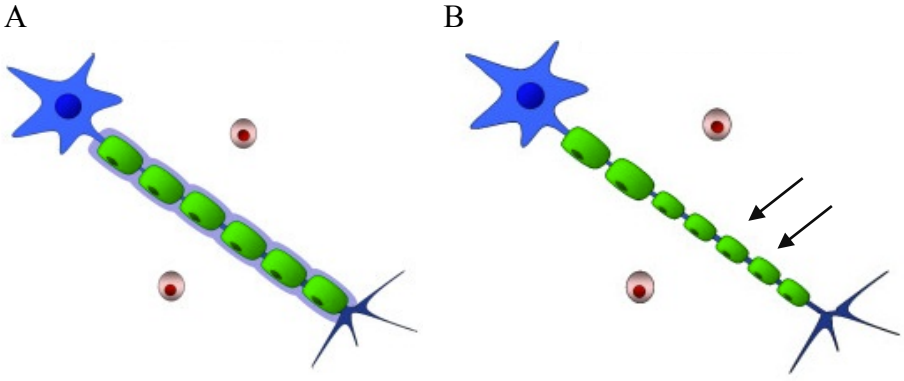

Figure 2.1- *A cartoon demonstration of myelinated and remyelinated axons. The healthy tissue with myelinated axon (panel A) has longer and thicker myelin compared to remyelinated axon (panel B). Arrows point to the remyelinated area of a previously damaged axon. Figure is obtained from Guadet et al, J Neuroinflammation, 2011(31) .*

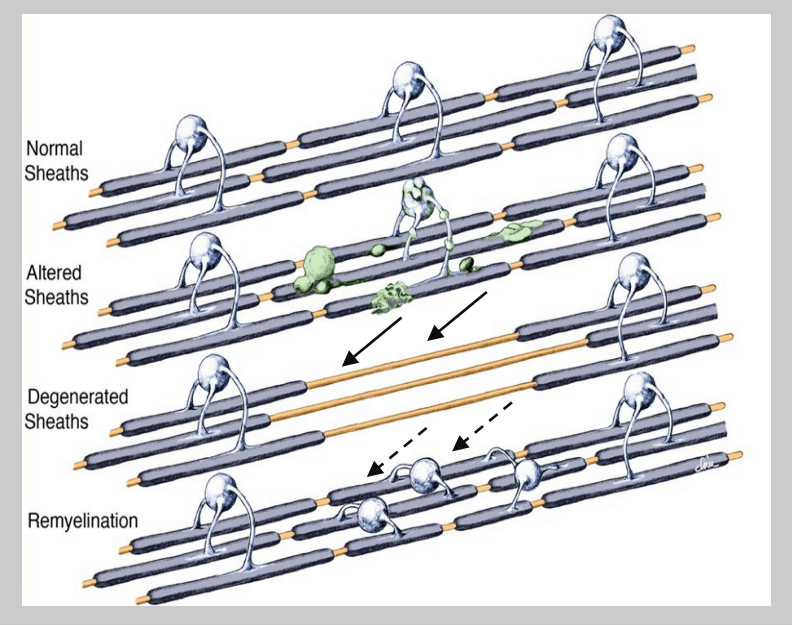

Figure 2.2- *Simplified schematic of de- and re-myelination in MS. Figure illustrates the structure of normally myelinated axons at the top. Arrows point out the demyelinated axons after injury. Following demyelination, restoration of myelin sheaths by oligodendrocytes is evident (dashed arrows). Figure is obtained and modified from Makoukji et al, Proceedings of the National Academy of Sciences of the United States of America, 2012 (32).*

Although remyelinated axons are covered with shorter and thinner myelin sheath (figure 2.1), myelin repair is thought to be critical for functional recovery in MS patients as it could enhance the conduction of action potential and protect axons against edema and ionic disturbances (33, 34). However, as demyelination progresses with disease chronicity, remyelination becomes insufficient and eventually fails in MS patients, and neurological deficit continues (35). Currently, there are no established means to predict how disease progresses in MS given its heterogeneity (36). Pathologically, it is also difficult to monitor the development of de- and re-myelination, as it is accompanied by several other pathological processes simultaneously in MS lesions (37). This calls for the use of animal models that allows for specific probe of myelination

property at dedicated locations.

2.3 Animal Models of Demyelination and Remyelination

In the study of MS, different animal models have been developed where different aspects of disease pathology can be studied. To evaluate de- and remyelination, at least two mouse models have been established: one with the local injection of lysophosphatidyl choline (LPC) or lysolecithin, and another by continuous feeding of cuprizone in the diet to the animals.

2.3.1 The Lysolecithin Model of De- and Re- myelination

Lysolecithin is a toxic, demyelinating agent that causes demyelination in white matter tracts, which is followed by spontaneous remyelination (38). The use of the lysolecithin model was first published in 1972 (39). By injecting 1 μl of 1 % lysolecithin in white matter tracts, extensive demyelination can be induced 7-14 days post injection, which is followed by a remyelination period 21-28 days after. These time periods may vary slightly depending on the mouse strain used. In the C57B/6 mice, remyelination can be delayed to 28 days following lysolecithin injection, in contrast to the 129Sv/Ev mice where remyelination is evident on 21 days. At the peak of demyelination, there may be loss of astrocyte and axons at the injection site (39).

The first experimental use of lysolecithin was in the cat and rat to study the electrophysiological properties of focally demyelinated and remyelinated axons (40, 41). Spatially, the dorsal column of the spinal cord at the thoracolumbar level for cat, rabbit, rat and mouse have been the usual targets of lysolecithin injection (42). The use of lysolecithin on any white matter tracts causes demyelination regardless of age, strain or species of the animals used (43). As an advantage of

this model, it is possible to observe de- and re-myelination in less than 30 days after induction of lesion. It is proposed that the detergent effect of the toxin on the myelin sheaths, not the oligodendrocytes, is the primary cause of demyelination, which was verified in immune deficient mouse and healthy models (39). Upon induction of lesions in the animals, infiltration of T cells, B cells and macrophages has been observed at the lesion location and is believed to have a positive role in the promotion of remyelination (42). The spatiotemporal predictability of lysolecithin lesions has made this model an ideal choice for in vivo studies of de- and re-myelination (44).

2.3.2 Curpizone Model of De- and Re- myelination

The cuprizone-fed mouse provides another model of demyelination and remyelination (45). Cuprizone, a copper chelator, refers to bis-cyclo- hexanone oxaldihydrazone, which initiates the inhibition of copper-dependent mitochondrial enzymes called cytochrome oxidase and monoamine oxidase (46, 47). This leads to cell apoptosis in the oligodendrocytes, which may be due to disturbances in energy metabolism (45). The corpus callosum is believed to be the primary target of demyelination in this model, although other areas such as superior cerebellar peduncles and the cortex have also been shown to have demyelination (46, 48, 49). The cuprizone model demonstrates extensive demyelination, axonal loss, and responses of microglia despite of an intact blood brain barrier (50, 51). The chelating agent is typically fed to 8-week-old C57B/6 mice for a period of 6 weeks with doses ranging from 0.2- 0.3% (w/w) to generate demyelination. After the peak of demyelination, spontaneous repair of damaged white matter occurs and can be further enhanced upon the removal of curpizone, leading to complete remyelination 2-5 weeks later (46, 52). As a result, it could take 8-13 weeks to observe de- and

re-myelination in this model, much longer than in the lysolecithin model.

2.4 MR Imaging Approaches of De- and Re-myelination

MRI is recognized as the standard imaging modality for assessing MS (53, 54). In this section, I have reviewed the type and roles of both conventional and quantitative MR imaging techniques with the potential to measure myelin property in MS. This is followed by a discussion of quantitative MR techniques based on image post-processing and analysis strategies.

2.4.1 Conventional MR Imaging

Clinically, conventional MRI is used for MS diagnosis, monitoring of disease progression, and for evaluating the effects of therapeutics. These include T_1- and T_2- weighted images as well as Gadolinium (Gd)-enhanced T_1 images.

2.4.1.1 T_1-weighted Imaging

T_1 MR imaging takes advantage of the longitudinal relaxation rate to detect tissue abnormalities (55). A large electromagnet is used in MR imaging to generate a magnetic flux density along longitudinal or Z-axis. Positively charged protons of hydrogen-containing molecules such as water are impacted by this magnetic field and align along the Z-axis. A radio frequency magnetic pulse is then applied perpendicular to this plane in order to excite hydrogen nuclei to another plane called the transverse axis (figure 2.3a). T_1 or spin-lattice relaxation is the time it takes the net magnetization to return to 63% of its original strength along the longitudinal axis.

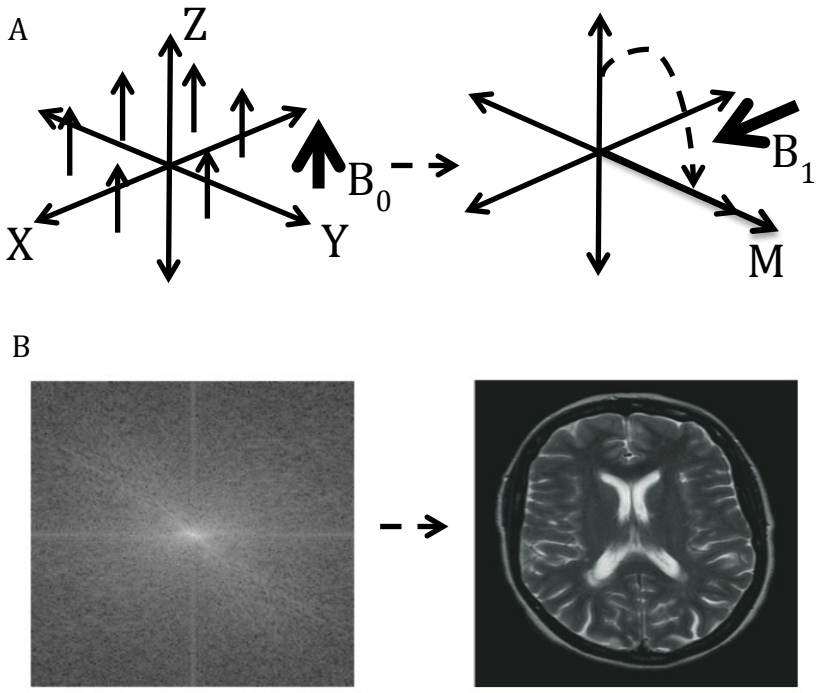

Figure 2.3- *A simplified flowchart of MR acquisition process. Panel A shows the equilibrium of magnetization of ^1H protons in presence of a main magnetic field B_0, followed by excitation of ^1H and rotation of magnetization (M) to the transverse plane upon induction of radio frequency pulse B_1. The recovery and decay of M is used to generate MR images with different tissue contrasts. Panel B shows the use of K space for the storage of raw data (in the frequency domain) and the use of inverse Fourier transform to generate the image in the spatial domain.*

Conventional MR techniques take advantage of the abundance of water in the body and the assumption that the proton of hydrogen (^1H) molecules of water and other molecules have different relaxation times in different environments and thus produce different imaging contrasts. Prior to having visible MR images, MR data is first collected in the frequency domain and then transformed to the spatial domain (figure 2.3b). In MS, many demyelinating lesions in T_1-weighted images appear as hypointense areas known as black holes, which are indicative of chronic neurodegeneration (56). In that regard, it is believed that hypointensity in T_1-weighted

images is correlated with severe myelin and axonal loss (57).

2.4.1.2 T_2 -weighted Imaging

T_2 or spin-spin relaxation time is the time it takes the net magnetization to decay to 37% of its original signal in the transverse axis. In T_2-weighted images, water components have a longer T_2 relaxation time than fat- and water-based tissues (58); therefore, demyelinating lesions in MS patients appear as hyperintense plaques in this MRI contrast. However, T_2 lesions lack specificity as T_2 hyperintensity could indicate inflammation, edema, gliosis and/or axonal loss, beyond de- or re-myelination (59, 60). In addition, T_2 lesion number or volume only correlates moderately with clinical outcomes of MS patients (61, 62).

2.4.1.3 Gadolinium-enhancement

Gadolinium- diethylenetriamine (Gd-DTPA) is a paramagnetic metal ion that enhances the relaxation of water molecules (63). In nerve tissue, Gd has greater effects on T_1 than T_2 due to the fact that T_2 relaxation, unlike T_1 relaxation, is largely due to the interaction of water and macromolecules (64). Therefore, presence of Gd in an aqueous solution and its binding to water molecules has a larger effect on T_1 by shortening its relaxation time. Consequently, the use of gadolinium creates a better image contrast compared to unenhanced T_1- or T_2 -weighted images for the detection of active demyelinating lesions, representing newly inflamed, and leaking blood brain barrier (65).

Despite the benefit of conventional MRI techniques, they lack specificity to pathology changes. Conventional outcome measures are mostly useful in detecting white matter lesions and tend to

underestimate the damages to the normal appearing tissue as they provide a limited measure of neurological dysfunction (53, 66). Hyperintense regions in T_2-weighted images are indicative of water presence in the area of interest, but does not specify whether this is due to inflammation, edema, remyelination or gliosis (67). Both de- and re-myelinated lesions appear as hyperintense in T_2-weighted images despite their pathological difference. Likewise, the analysis of T_1 hypointense areas does not reveal information about the specificity of the underlying pathology; although hypointense lesions have been shown to return to isointensity after periods of active inflammation, this is thought to be due to remyelination and/or reduction in edema (68).

2.4.2 Quantitative MR Imaging:

Quantitative MR measures have the potential to improve the specificity of lesion pathology (69, 70). Over the past decades, several quantitative MRI techniques have been developed including magnetisation transfer imaging, myelin-water imaging, susceptibility-based imaging and diffusion tensor imaging. Each has demonstrated myelin-associated information, which is reviewed in the following sessions.

2.4.2.1 Magnetization Transfer Imaging

Magnetization transfer imaging is a semi-quantitative MR technique that takes advantage of signals from mobile and restricted hydrogen protons to generate information about an in vivo pathology. This approach uses the effect of magnetization coupling between mobile hydrogen protons and motion-restricted hydrogen protons affiliated with macromolecules such as lipid-rich myelin. Theoretically, the spin state of free protons like that of water can be affected with the spin state of restricted protons. This could be used, indirectly, to gather information about the

state of semisolid, non-mobile macromolecules such as the myelin sheath. Based on this concept, magnetization transfer imaging offers a measure known as magnetization transfer ratio (MTR). MTR is calculated based on the ratio of the difference in signal intensity before and after the use of a radio frequency pulse that saturate the macromolecule magnetization. This measure has been used in MS research to measure the content of myelin (71) (Figure 2.4).

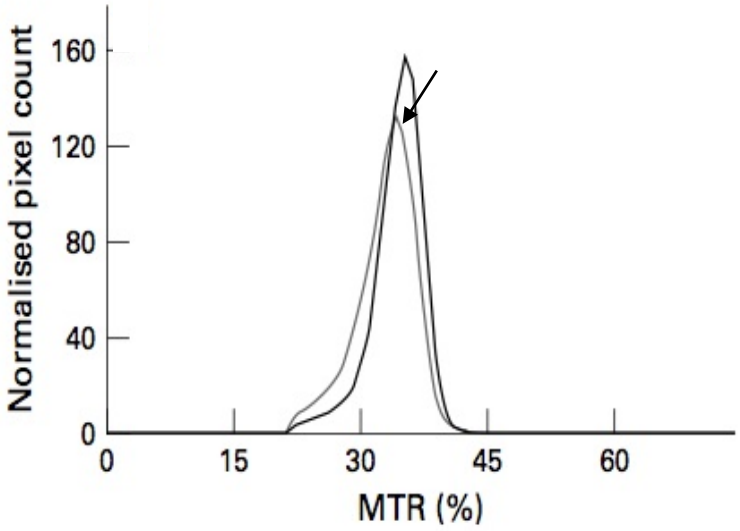

Figure 2.4- *Magnetization transfer ratio histogram of normal appearing white matter in MS patients (grey line) and healthy controls (black line). As the arrow indicates, there is reduced MTR for the normal appearing white matter as compared to the healthy tissue. Figure is obtained from Cercigani et al*, *Journal of Neurology, Neurosurgery & Psychiatry*, *2001* (72).

MTR has been used in MS in a variety of applications. Several studies have reported reduced MTR in the normal appearing white matter (NAWM) and MS lesions compare to the healthy tissue (71, 73). Furthermore, MTR has demonstrated the ability to predict clinical disability and evolution, which is not predicted by conventional imaging (74, 75). After a 5-year follow-up with MS patients, strong positive correlation was found between changes in clinical disability

scores and MTR evaluations in normal appearing white matter. MTR has shown promise in detecting remyelination in MS lesions (76). In this regard, a Canadian-based study found significant MTR increases during a 7-month period after lesion enhancement, which was suggested to be associated with remyelination (77). Despite its potential, several limitations are reported in the use of magnetization transfer imaging. One of the concerns is the inter scanner variability of MTR, due to several factors such as the use of different scanners and pulse sequences (78). Moreover, while the reduction in MTR is suggestive of myelin damage, it may also be due to inflammation and axonal damage (79, 80).

2.4.2.2 Myelin-water Imaging

A multi component T_2 relaxometry technique called myelin-water imaging has also shown potential to measure the myelin content. Myelin-water imaging uses the difference between T_2 relaxation time of water trapped within myelin layers and the water from other regions of the central nervous system to evaluate myelin content (figure 2.5) (81). This is based on the concept that hydrogen protons of water in these environments have different relaxation characteristics. Using this approach, a measure called myelin-water fraction (MWF) was derived. MWF is defined as the ratio of myelin-water signal to the total water signal from the rest of CNS tissue.

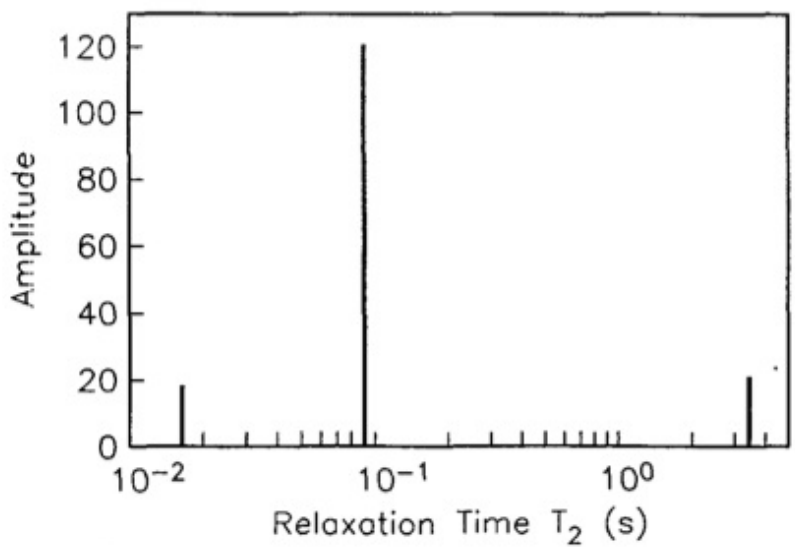

Figure 2.5- *T_2 relaxation distribution corresponding to cerebrospinal fluid (right-most signal), intra- and extra-cellular water (middle signal) and myelin water (left signal) trapped tightly between the myelin bilayers. Figure is obtained from Mackay et al, Magnetic Resonance in Medicine, 1994 (82).*

Myelin-water imaging has been used to detect myelin in a variety of studies in MS (figure 2.6). In a quantitative study of MS brain samples, strong positive correlation was found between the density of stained myelin and MWF (83). Another study compared the MWF of MS lesion, NAWM and normal white matter and found lower MWF in lesions than in the NAWM (84). This research also showed that NAWM had a lower MWF compared to the normal white matter, suggesting that NAWM has a globally demyelinated pathology. A recent study evaluated the change in MWF in new enhancing and non-enhancing MS lesions (85). The authors suggested that although early MWF decreases were associated with edema, longitudinal assessment of MWF in MS lesions may be used to evaluate the degree of remyelination (85). This study was based on three new MS lesions. Some researchers also suggest that MWF is insensitive to axonal

damage and inflammation, making it suitable to evaluate myelin content in MS (86). However, myelin water imaging may not be able to distinguish myelin debris from the intact, healthy myelin, and the exchange rate of water molecules between multilayer structures of myelin could impact the measure of MWF (87-89). In addition, this technique may also suffer from long acquisition time, making its transition to clinical use challenging (90).

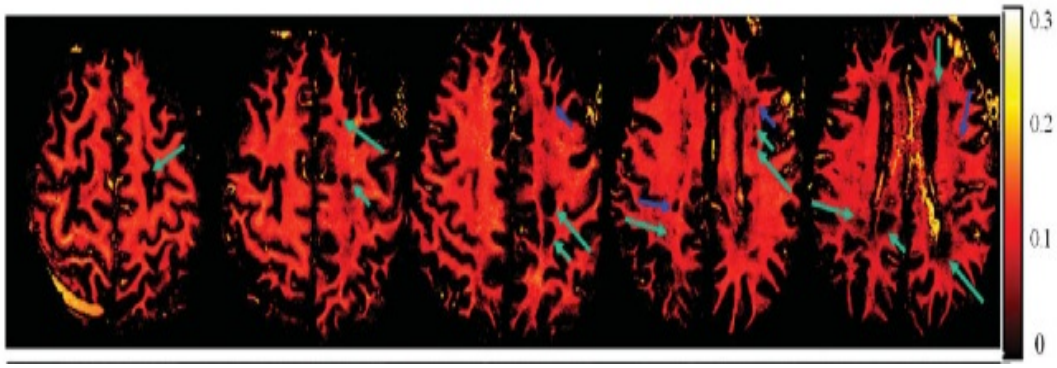

Figure 2.6- *Myelin-water fraction maps of an MS patient's brain. Arrows point out the location of lesions with severely diminished myelin-water fraction, appearing as dark areas. The color-coded scale shows the numerical myelin-water fraction. The figure is Obtained from Du et al, Magnetic Resonance in Medicine, 2007 (91).*

2.4.2.3 Diffusion Tensor Imaging

Diffusion tensor imaging (DTI) has been used to characterize the microstructural properties in MS in a variety of studies. DTI assess the free movement of water molecules along nerve fibers to determine the degree of restricted diffusion based on the concept of Brownian motion (92). Based on the alignment of tissue microstructure and the directionality of nerve fibers, DTI has demonstrated promise to measure tissue microscopic pathology with a macroscopic appearance. Common DTI indices include fractional anisotropy (FA), mean diffusivity (MD), as well as axial

and radial diffusivity. FA describes the degree of anisotropy in diffusion, where a value of 0 indicates equal diffusion in all directions and a value of 1 represents diffusion along one direction. MD refers to the average of diffusivity regardless of directions. Axial diffusivity refers to the degree of diffusion along the major axis of nerve fibers in a 3D plane whereas radial diffusivity is the average of other two minor diffusion axis in the 3D plane (figure 2.7).

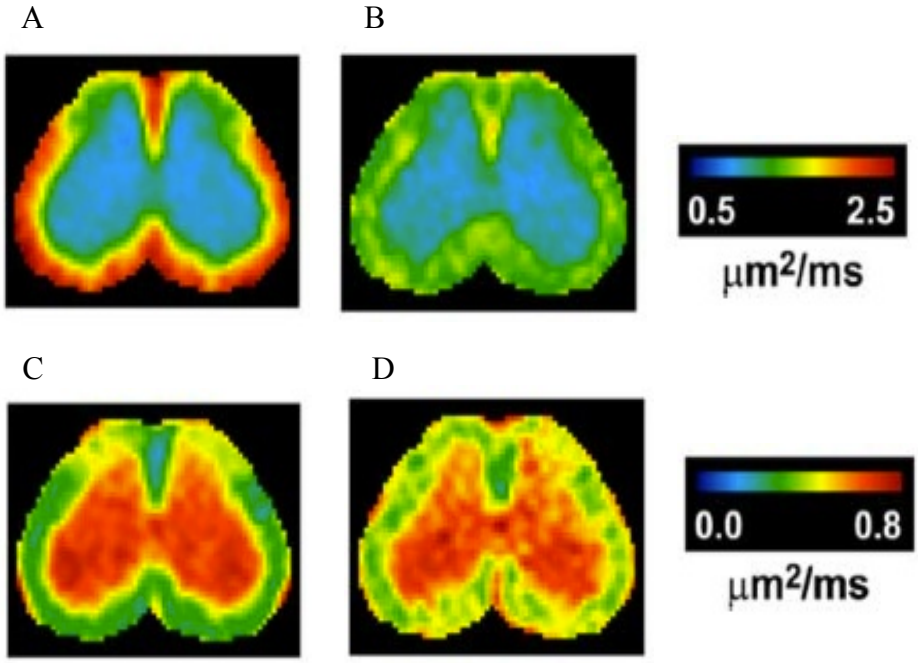

Figure 2.7- *Axial (top row) and radial (bottom row) diffusivity of the spinal cord in a animal model of MS before the development of clinical symptoms (panel A,C) and after having maximum disability (panel B,D). The change in DTI indices of the dorsal column illustrates the increase in the severity of demyelination. The legend shows the rates of diffusivity and their corresponding colors. Figure is obtained and modified from Budde et al, the Journal of Neuroscience***,** *2009* (93).

DTI has been used to detect myelin and axonal integrity in both MS and its animal models. A recent study showed significant increase in the radial diffusivity and decrease in the axial diffusivity of dorsal column lesions in rat spinal cords compared to the healthy white matter, indicating increased tissue pathology (94). Based on positive correlation of radial diffusivity and histo-chemically stained tissues, a DTI study showed that radial diffusivity could serve as a marker of overall tissue integrity in chronic lesions of spinal cord of MS subjects (95). To evaluate the extent of repair in gadolinium-enhancing lesions, Fox et al measured the changes in radial diffusivity among 21 MS patient over one year (96). Their results suggested that the decrease in radial diffusivity could be due to remyelination. Nonetheless, some studies have also reported that an increase in radial diffusivity may not be entirely due to changes in myelin integrity (94, 95). In addition, the elimination of inherent crossing fibers due to axonal damage could improve voxel anisotropy and alter the true FA. Consequently, DTI may help us infer the anisotropic properties of tissue microstructure, which are important for a better understanding of overall tissue integrity, but DTI measures may not be necessarily specific to de- and re-myelination.

2.4.2.4 Quantitative Susceptibility-based MRI

Susceptibility-weighted imaging uses the difference in MRI susceptibility between tissues to create image contrast. The term susceptibility refers to distinct magnetization responses of different tissues when they are exposed to magnetic field. This technique combines the phase and magnitude data to create a MR image. Quantitative susceptibility mapping is a method that uses Larmor frequency shift to evaluate the degree of disease activity by assessing the degree of iron accumulation and demyelination where both processes lead to a higher positive susceptibility in

a tissue. As a diamagnetic substance, myelin experiences a reduced Larmour frequency when it is exposed to an external magnetic field (97). The shift in the inherent frequency is orientation-dependent and can be mapped and evaluated. In addition, the lipid molecules that give rise to the unique structure of myelin are magnetically anisotropic, which gives rise to a relationship between susceptibility contrast and myelin-based microstructure orientation (98)(figure 2.8). The images that have been generated using these techniques have a great contrast-to-noise ratio, and have the ability to visualize paramagnetic and diamagnetic tissues better than the traditional MRI contrast mechanisms.

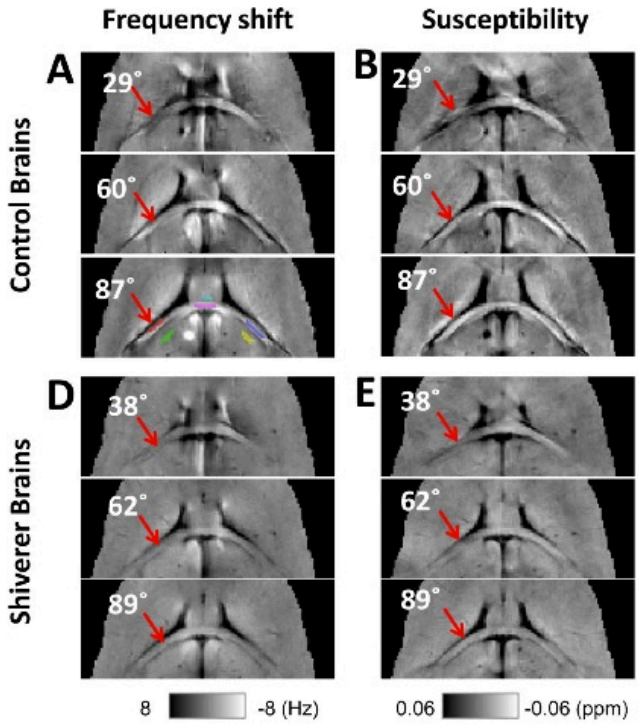

Figure 2.8- *Dependence of magnetic susceptibility on tissue orientation in normally myelinated and dysmyelinating shiverer mice. Panels A and D show the frequency maps from brain orientations while panels B and E show the magnetic susceptibility due to the frequency shifts*

shown in A and D. Susceptibility anisotropy is observed in the control mice but not in shiverer mice. Figure is obtained from Li et al, NeuroImage, 2012 (98).

Susceptibility-weighted imaging has been tested to detect myelin content. A study in mice showed that the loss of myelin in brain leads to the reduction of white matter magnetic susceptibility, thereby introducing quantitative magnetic susceptibility as an endogenous marker for myelin content (99). Another study used quantitative susceptibility mapping to evaluate tissue changes in white matter of MS patients and found that there was significant correlations between quantitative susceptibility and the Extended Disability Status Scale (100). Based on the concept of anisotropic susceptibility of phospholipid bilayers of the myelin sheath, a postmortem study of human corpus callosum showed that tissue susceptibility is sensitive to changes in tissue microstructure and orientation relative to the main magnetic field (101). They found that the resonance frequency of oriented samples changed with their position (parallel or perpendicular) relative to the magnetic field. This suggests the improved potential of susceptibility imaging to evaluate tissue micro-organization and compartmentalization compared to conventional imaging. However, the transverse relaxation rate of quantitative susceptibility lacks specificity as greater degrees of iron and myelin may lead to greater relaxation rate (102, 103). Therefore, the use of quantitative susceptibility to evaluate myelin content needs to be further validated.

2.5 Image Processing and Analysis of De- and Re-myelination

Aside from MR acquisition techniques, image processing and analysis strategies may become alternative methods to detect characteristics of demyelination and remyelination. Image processing and analysis utilizes mathematic algorithms to extract information from acquired MR

images. Several potential approaches are reviewed below.

2.5.1 Frequency Distribution and Tissue Injury and Repair

As described in the beginning of the imaging sections, MR data are originally acquired in the spatial frequency domain, which are converted to the visible MR images through the application of inverse Fourier transform (FT) (104). The FT refers to a series of mathematical manipulations that transform the MR images back to the frequency domain. Theoretically, any type of complex signal can be represented by a combination of wave forms through FT. Specifically, the FT of an image is the combination of sine and cosine waves with various frequencies enclosed in the image, represented by the organizing pattern of pixel intensities in MRI. The distribution of MRI frequencies can then be analyzed for their distribution and directions in order to assess the property of the underlying tissue (105) .

2D FT can compute the map of local oriented structures in digital images by decomposing image content into frequencies with varying amplitude on a 2D grid (106). Based on this approach, uniform structures with preferred orientations in an image appear as high amplitude frequencies along a direction in 2D Fourier transformed images (107). Based on a geometrical representation, tissues with a higher degree of fiber organization have an elliptical FT distribution, which is characteristic of the anisotropic nature of the underlying tissue microstructure. Quantification of geometrical properties of the ellipse such as the major and minor axes could be used as measures of tissue integrity in the frequency domain of an image (figure 2.9).

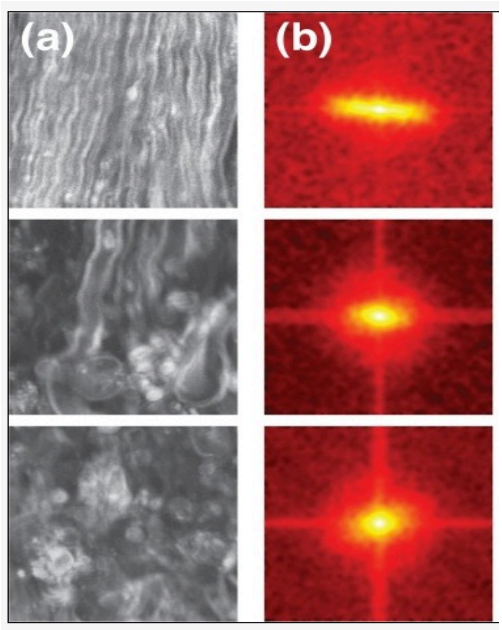

Figure 2.9- *Spatial and frequency domain images of spinal cord from an experimental autoimmune encephalomyelitis (EAE) model of MS. Microscopy images of a mouse spinal cord from a longitudinal view (panel a). The progress of EAE and its impact on tissue alignment is shown from top to bottom (healthy to diseased). Panel b shows the processed 2D-FT images, illustrating an almost anisotropic (ellipse) structure for the healthy tissue followed by less elliptical structure (shift toward isotropy) in the damaged cord. The figure is obtained from Chamma et al, Biomed Opt Express, 2013 (108).*

2D FT was used to quantify the preferred orientation of collagen in various biological tissues (107). This article based its computation of collagen tissue direction on distribution of frequencies in the Fourier domain and suggested that collagen of trachea tissue has the highest degree of directional distribution compared to ear tissue. Another study used the same methodology to evaluate the orientation of collagen in healthy and malignant breast tissue (109). In this study, the authors evaluated the directional properties of tissues and found significantly better cellular organization for the healthy controls compared to cancerous tissues. Very recently,

a 2D Fourier transform-based measure was used to evaluate the myelin integrity in the experimental autoimmune encephalomyelitis (EAE) animal model of MS (108). In this study, 2D FT was applied to microscopy images of EAE lesions to quantify the fiber orientation and myelin health of animals with varying degrees of clinical disability. Based on post-processing of histology images in this study, the authors developed an outcome measure that quantified fiber structure and the directional organization of tissues with different myelin content. This suggests the potential of 2D- FT analysis for evaluating the myelin content in MS-like lesions based on tissue directional properties.

2.5.2 Image Texture Analysis

Image-processing strategies such as texture analysis allow for the extraction of quantitative information from a variety of MR images. In MS, it is often challenging to detect subtle pathological changes. Using MRI texture analysis, researchers found significant difference between MS lesions and healthy tissue (110). Image texture refers to a characteristic distribution of pixel intensities (darkness and brightness within an image) that can provide us with invisible information about the arrangement of structures in an image (111, 112). Texture analysis can be done using several approaches, one of which is based on the spatial frequency in an image. Recently, a local spatial frequency-based strategy known as Stockwell transform has shown improved sensitivity compared to FT-based methods (113).

The promise of MRI texture analysis using this and other techniques has been shown in various neurological diseases including MS. Quantification of subtle changes using texture analysis has been made possible in studies of epilepsy (114-116), brain tumours (117, 118), MS (119-122)

and Alzheimer's disease (123). Indeed, studies have shown the effectiveness of texture analysis in detecting microstructural changes in early stages of MS (124). A very recent article by Zhang et al using the Stockwell transform method showed that the heterogeneity of MRI texture correlated with the severity of MS pathology, indicating the ability of advanced image analysis to detect tissue integrity that is not possible by human eye (125). The specificity of texture analysis to de- and re- myelination is shown in animal models, and its potential in human studies is to be validated (14).

2.5.3 Structure Tensor Analysis

Structure tensor analysis is a new image post-processing strategy that may have the potential for assessing de- and re-myelination. Unlike texture analysis, which evaluates tissue pathology based on the spatial organization of pixel intensities, structure tensor analysis uses the variation in pixel intensities to estimate structural property, especially on tissue directionality (61, 126). The tensor of a structure refers to its directional gradients along predominant orientations, namely, eigenvectors. The strength of an eigenvector is measured by a scalar known as eigenvalue. Structure tensor analysis determines the eigenvector and eigenvalues and their similarities based on a 2-dimensional (2D) tensor matrix, f(x,y), derived from the image, where f(x,y) defines the two dimensions of the image in the x and y directions (127) (Figure 2.10). For example, given an image J, the direction of the unit vector in the image is specified by u_θ $\nabla f(x,y)$, where the gradient of pixel intensities in 2D , $\nabla f(x,y)$, is used to find the dominant directions. Finding the direction along u is maximized and that gives the structure tensor of J. The first eigenvector of J dictates the dominant orientation in the image with an eigenvalue of λ_{max} , followed by a second eigenvector in the orthogonal direction with an eigenvalue of λ_{min},

representing the minimal direction. The eigenvalues of the dominant and minimal eigenvectors are used for the calculation of coherency and energy in this project.

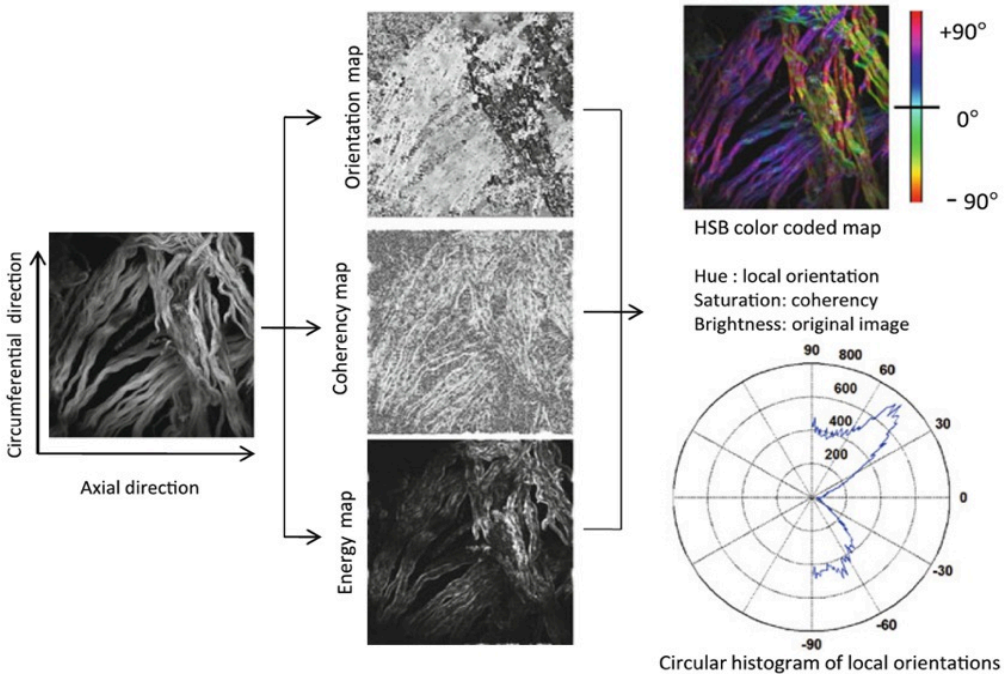

Figure 2.10- *Flowchart of structure tensor analysis, illustrating different tissue directional properties as outputs. Coherency, energy and orientation maps were used to visualize the directional properties of local tissue structures. A Color-coded image and its corresponding angular histogram were generated to showcase different angle distributions. Figure is obtained from biomedical imaging group, 2014 (OrientationJ).*

Several studies have used structure tensor analysis to evaluate tissue directionality and anisotropy. He et al have used structure tensor based parameters to assess the properties of collagen and elastin fibers in articular cartilage of kangaroos (10, 128). They studied the effect of mechanical strain and its impact on the dominant orientation, orientation distribution and

coherency of collagen and elastin within different layers of cartilage tissue. They found that the overall structure and organization of elastin and collagen changes based on degree of strain applied. Likewise, Rezakhaniha et al investigated the response of adventitia to mechanical stress and its impact on collagen orientation and structural distribution using structure tensor analysis in carotid arteries of rabbits (11). They identified four distinct groups of fibers with specific orientations with respect to the axial direction of the artery. A recent study investigated the architecture of rat ventricles by evaluating laminar orientation of complex myolaminar structures (129). They compared the accuracy of DTI MR and structure tensor of myolaminar orientation against manual measurements and found that structure tensor is a better measure of myolaminal orientation. Recently, structure tensor analysis has also been used to verify the results of fiber orientation analysis investigated by DTI.

Structure tensor analysis has also been explored to evaluate tissue orientation in the central nervous system. In a 2012 article, Budde et.al used structure tensor analysis to quantify the anisotropy of fiber orientation in rat brain using histological sections; the goal was to verify the results of DTI in the same sample (130). They found that there was a strong positive correlation between structure tensor analysis-based measures in histology and those using DTI, showing the ability of structure tensor analysis to evaluate structural organization. The same research group used structure tensor analysis to evaluate and orientation and anisotropy of human brain sections (12). They found that tissue anisotropy was lower in areas with higher density of crossing fibers compared to areas with more coherent fiber bundles, such as corpus callosum. A more recent study investigated the neuronal fiber orientation of macaque cortex using structure tensor analysis in histological images and compared the findings with those derived from a model-

based analysis of 3D diffusion-weighted MRI (131). Consistent results were shown between these two approaches despite the difference between plane dimensions (2D versus 3D), supporting the potential of structure tensor analysis as compared to advanced acquisition approaches. However, no research has been done using structure tensor analysis to assess demyelination and remyelination in MS or other diseases. This becomes the focus of my thesis, in which I used a well-defined animal model of de- and re-myelination to examine the utility of this method as shown in the following chapters.

Chapter Three: **Assessing the Potential of Structure tensor Analysis to Measure Myelin Integrity in Mouse Spinal Cord Verified with Histological Images**

3.1 Introduction

Changes in myelin integrity of nerve fibers characterize the pathology of MS lesions, but it is difficult to detect myelin component alone in these lesions, as they are characterized by complex and intervening pathological processes (132). To accurately measure the degree of demyelination and subsequently of remyelination in MS and other demyelinating diseases, the availability of quantitative methods is highly desirable, especially those with histological validation. In this regard, animal models with well- characterized myelin activity are needed, where demyelinated lesions can be explicitly localized.

Currently enormous efforts have been made to develop quantitative measures of structure directionality associated with tissue integrity. One such candidate is DTI, which estimates tissue integrity based on the diffusing preference of water molecules. Recently, based on post-processing of existing images, structure tensor analysis shows potential for assessing tissue alignment and anisotropy using existing images. Analogous to diffusion tensor, structure tensor of an image generates a series of alignment metrics based on mathematical calculation of tissue directionality (127). In particular, this technique identifies the coherency (anisotropy), energy (trace of dominant directions to evaluate organization), and angular entropy (composition of structure directions) in a tissue. The promise of structure tensor analysis has been shown in several studies, but evaluation of the coherency in myelin content has not been done (10, 12, 128, 130, 133).

In this study, I used structure tensor-based analysis to examine the coherency and anisotropy of normal white matter, and partially and completely demyelinated white matter in histological images of mice spinal cords. I hypothesized that the directional properties of these structures differ and that the differences can be detected using directionality-derived measures.

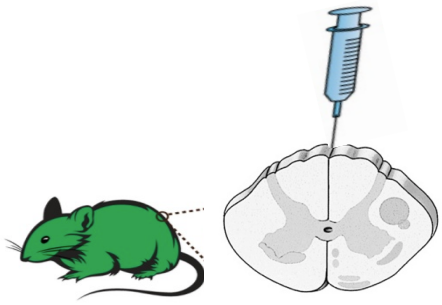

Figure 3.1- *A simplified schematic of how the lysolecithin model of demyelination is developed. The deposition of lysolecithin into the dorsal column of the exposed mouse spinal cord is shown. The figure is obtained and modified from Lacroix et al, PloS one, 2014 (134).*

3.2 Methods

3.2.1 Animal Model

The lysolecithin model of demyelination was used to provide histological images for my analysis. Thirteen C57B/6 mice were anesthetized with a mixture of ketamine and xylazine; the spinal cords were then exposed. Demyelination was induced in the dorsal column of thoracic spine by injection of 1 µL at 1% solution of lysolecithin (figure 3.1) (13). The needle was left in the tissue for additional 1-2 minutes to avoid backflow of the lysolecithin. Following surgery, animals were allowed to recover for at least 7 days while their sutures were checked on daily bases, with food and water provided as usual. During this period, demyelinated lesions were induced in the injury sites of these animals. Subsequently, the mice were sacrificed and perfused

with 4% paraformaldehyde at 4° C temperature before their cords were removed for histological sectioning (13).

3.2.2 Sample Preparation

To evaluate myelin content, 10 μm-thick axial sections of the spinal cord were cut around the lesion center and stained with luxol fast blue (LFB), and then were imaged for analysis. Histological images at the lesion epicenter and at a distant site 500-μm away from the epicenter were collected for each animal. Three tissue types in each histological image were studied: healthy white matter with intact LFB, which was referred to as non-demyelinated or healthy tissue; completely demyelinated areas within a lesion with complete loss of LFB stain; and the border area or partially demyelinated tissue (partial loss of myelin stain; Figure 3.2). Images that were not properly stained, with lesions outside of the dorsal column or looked blurry were excluded.

3.2.3 Image Pre-Processing

An open source image-processing program named ImageJ (NIH, version 4.7) was used to conduct the pre-processing of histology images. The original color images were first converted to three gray-scale images (red, green and blue), and then the gray-scale image with the best contrast, which was the red image, was chosen for further analysis. As inhomogeneity in the staining intensity is a common issue in histological images, I normalized the chosen images by setting a common saturation threshold of 0.4% for all images through the ImageJ program. However, we tested the coherency measure in both normalized and non-normalized images and found no significant difference before and after normalization.

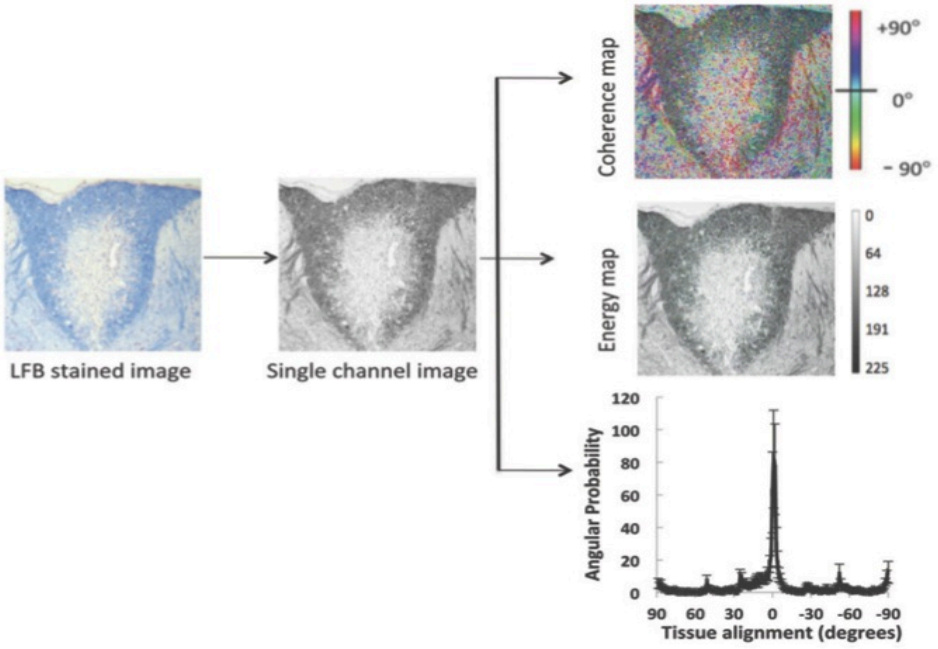

Figure 3.2- *A representative flow chart showing the steps we performed to quantify the orientation outcome (coherency, energy and entropy) using a high contrast grey scale image. The grey scale image was obtained after the preprocessing of the luxol fast blue – stained histology image (left panel) from the dorsal column of a mouse spinal cord was decomposed into 3 gray scale images. The red channel image that showed the best anatomical contrast (middle panel) was selected for structure tensor analysis, from which the coherency (top, right panel) and energy (middle, right panel) maps from the whole image, and the angular distribution from a region of interest of healthy white matter (bottom, right panel) was obtained.*

3.2.4 Image Analysis

Structure tensor analysis was performed using an ImageJ plug-in (OrientationJ) to derive the coherency, energy and angular entropy outcomes (11). In each image, we identified 2 to 7 regions of interest (ROIs) per tissue type. The size of the ROI was chosen based on the size of the stained regions and the efficiency of the ROI sizes to cover sufficient tissue areas. ROIs were

approximately 7 x 7 μm in each tissue. Based on my prior experiments (personal observation), smaller ROIs were not sufficient for directional analysis while larger ones did not provide complementary information compared to the size of ROIs used here. The energy measure is calculated based on the sum of maximum and minimum eigenvalues of in the ROI. The coherency is defined as the ratio of the difference between maximum and minimum eigenvalues to their sum. Based on the coherency and energy, I created color-coded images to assist for visualization (Figure 3.3); numerically, higher coherency and energy corresponds to greater anisotropy and better tissue organization. I calculated the entropy of all tissue types to evaluate the degree of tissue disorder. This was based on the angular distribution of tissue microstructure. A histogram of structure directions as a function of their frequency was generated. Within a ROI, the structure directions had a range of -90 to +90 degrees, reflecting the probabilistic distribution of all orientations (Figure 3.3). The entropy, ε, was defined as: $\varepsilon = -\Sigma$ [log p (θ) x p (θ)] where $p(\theta)$ represented the probability of oriented structures that had a similar angle (θ) to the dominant direction of the ROI (135). For an oriented tissue, more negative entropy corresponded to more anisotropic structures, and thus a less disordered, heterogeneous ROI.

3.3 Statistical Analysis

A linear mixed-effect model was used to evaluate differences in coherency, energy, and angular entropy. This model accounts for the variability between mice and histological images beyond the inherent pathological variation. Specifically, outcome differences between tissue types, both from all samples and at lesion sub-locations were compared. For the lesion and border tissues, the difference between epicenter and distant sites of the injury was compared. I normalized the outcomes by measures of the he∇althy tissue within the image. All the analyses were conducted

using Stata 12 where a $p < 0.05$ was considered to be significant.

3.4 Results

3.4.1 Sample Characteristics

After the initial assessment of the images from 13 mice, images from 9 were included based on the criteria previously stated; 7 mice had images from both epicenter and distant sites of the injury, and 2 mice had images from the epicenter only. In total, we analyzed 16 histological images (2048 x1536 pixels). Overall, 178 ROIs were assessed: 72 in the healthy tissue (non-demyelinated), 57 in the lesion border (partially demyelinated), and 49 in the lesion (demyelinated) completely (table3.1).

Table 3.1- *The number of regions of interest (ROIs) per mice, image, and tissue type. (Note: Under Image category, number 1 represents the epicenter and 2 the distant area of the lesion)*

Mouse	Image	Number of ROIs		
		Healthy	Lesion	Border
1	1	7	4	4
	2	7	5	4
2	1	3	4	4
	2	6	4	4
3	1	4	4	4
	2	5	2	4
4	1	5	4	4
	2	4	4	4
5	1	3	3	4
	2	5	4	4
6	1	5	4	4
	2	4	2	3
7	1	4	2	3
	2	2	1	1
8	1	2	2	2
9	1	4	2	4

3.4.2 There Was Significant Difference in Each Measure When All the Samples Were Considered

As shown in the color-coded images (Figure 3.3), extensive loss of color saturation (green) for coherency and energy (blue) were noted in the demyelinated lesion compared to the partially demyelinated tissue at lesion border; the myelinated, healthy tissue with intact LFB stain showed the strongest coherency and energy as per color saturation. Consistent with this analysis, the angular distribution of the healthy tissue was dominated at 0 degree with little spread at other angles; in contrast, the nerve fibers were oriented at various degrees in both border and lesion tissues, and no preferable angles were identified. This appeared more prominent in lesions than in the border tissue. Quantitatively, I found that coherency in the non-demyelinated tissue (mean ±standard error = 0.23 ± 0.01) was significantly better than in the completely demyelinated (0.08 ± 0.01, $p < 0.01$) and border tissues (0.14 ± 0.01, $p < 0.01$) (Figure 3.4); border coherency was also greater ($p < 0.01$) than that of completely demyelinated lesions. The energy outcome was also greater both in the healthy (122.96 ± 10.24, $p < 0.01$) and border (131.69 ± 10.38, $p < 0.01$) tissues compared to the completely demyelinated lesions (40.27 ±4.16), but there was no significant difference between border and healthy tissues ($p = 0.10$). In a similar trend, the angular entropy was the highest in lesions (-29.97 ± 4.32) compared to the healthy (-107.91 ± 13.62, $p < 0.01$) and border tissues (-80.75 ± 11.10, $p = 0.01$); no difference was detected between healthy and border tissues ($p = 0.26$).

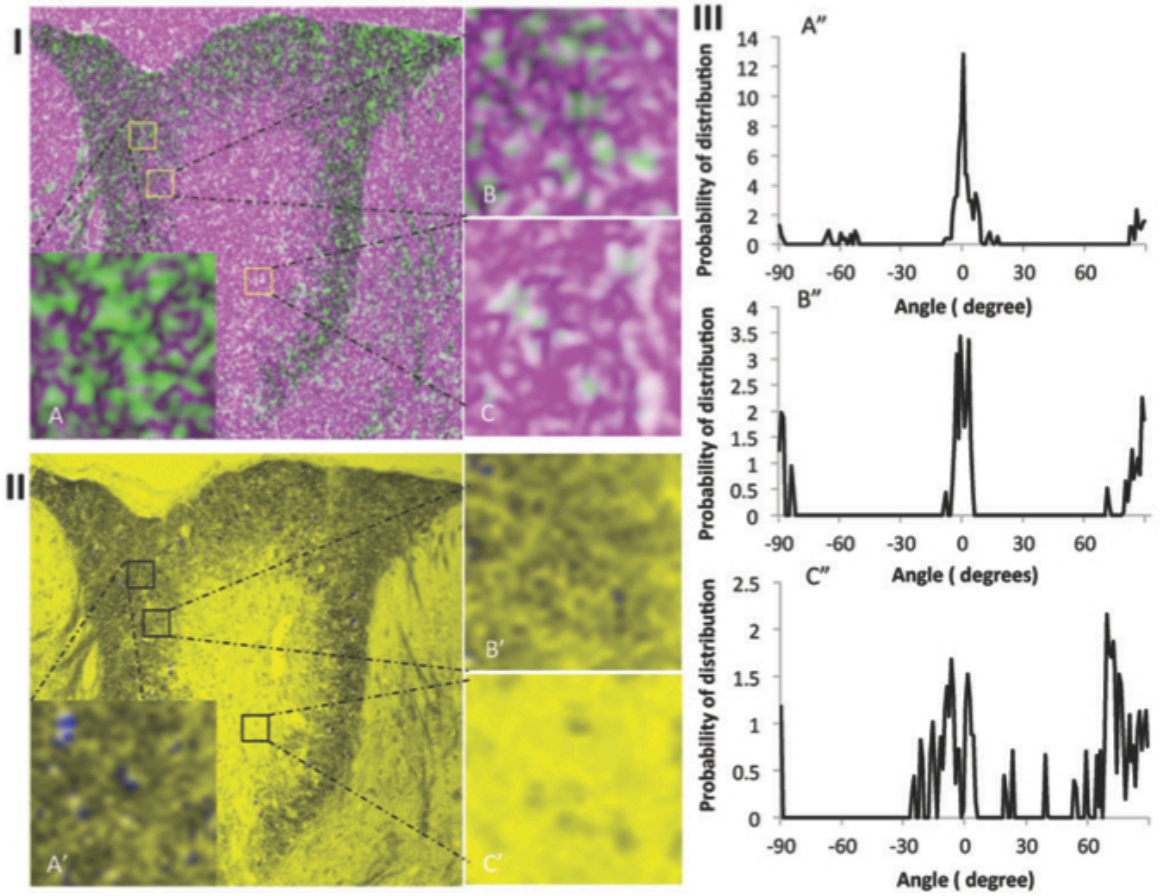

Figure 3.3- *Examples of coherency (I) and energy (II) maps and tissue angular distributions (III) from the healthy (A, A', A''), partially demyelinated (B, B', B''), and completely demyelinated tissues (C, C', C''). In panel I, coherency is represented by green that is seen decreasing from A to B and to C. In panel B, blue represents energy that demonstrates a similar distinct pattern (A' to B' to C') as in panel I, but at a lesser extent. In panel III, the alignment of healthy white matter (A'') is concentrated at 0 degree, while the partially demyelinated tissue (B'') is dispersed along both -90 and +80 to 90 degrees, beyond 0 degree; further, in the lesion tissue, tissue direction is dispersed from -30 to +90 degrees, with only a minor peak at 0 but a large one at +80 degrees. Zero degree describes the dominant orientation of structures oriented in the dorsal column of mouse spinal cord with intact myelin content.*

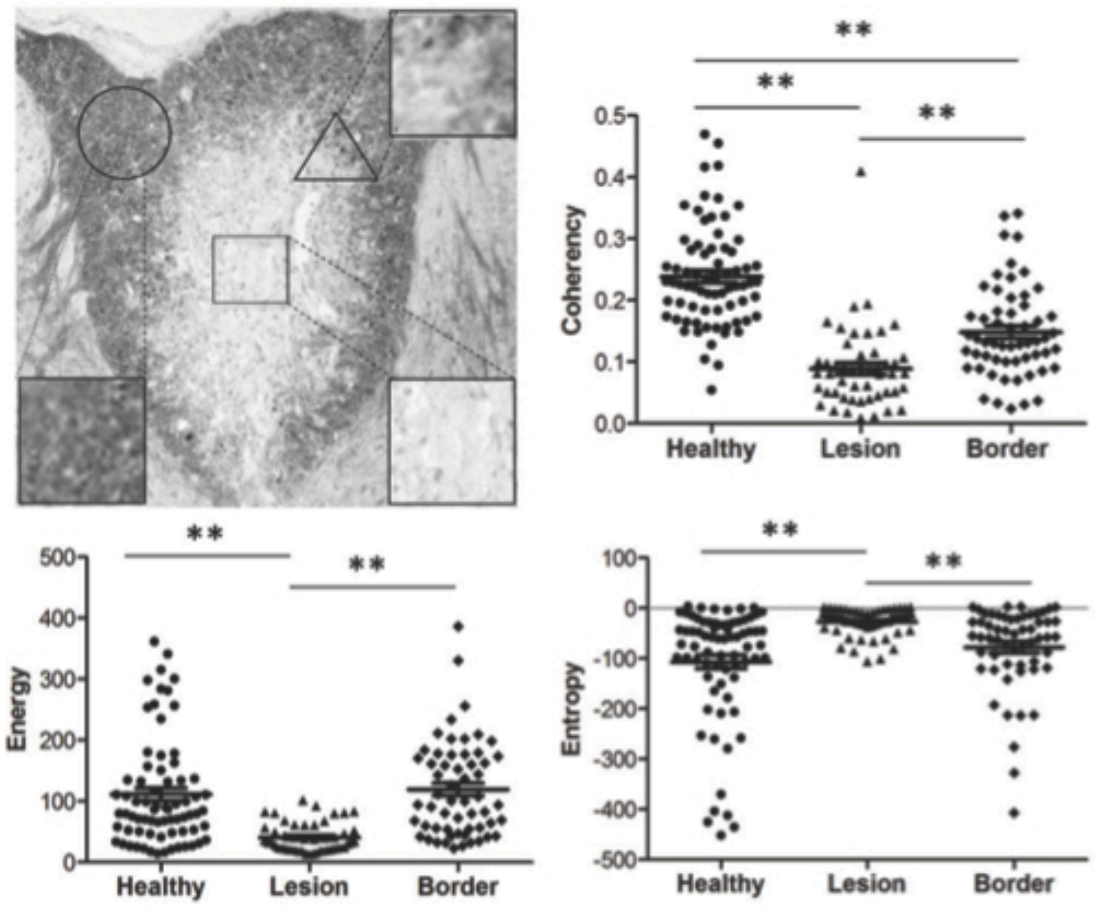

Figure 3.4 -*Example regions of interest (A) and the scatter plots of coherency (B), energy (C), and entropy (D) outcomes from the healthy (circle), partially demyelinated (triangle) and completely demyelinated (square) tissue from all samples. There was significant difference (p< 0.01) between tissue types in each measure, especially between lesions and the healthy tissue. Bars represent 95% confidence interval and standard errors.*

3.4.3 Consistency of Tissue Differences at Both the Epicenter and Distant Sites of the Injury

Deposition of lysolecithin into the dorsal column of the spinal cord can cause extended demyelination along the cord, ranging from to 2-4 mm (unpublished observations). Using the

mixed-effect model, the difference between tissue types at different sites of the injury was assessed. At both the epicenter and distant locations of the injury, the coherency of healthy tissue was the highest compared to other tissues, and the coherency of the border tissue was higher than completely demyelinated lesions ($p < 0.05$). In energy and entropy, the difference between healthy tissue and lesion, and between lesion and border tissue, was detected ($p < 0.05$); however, there was no difference between border and healthy tissue (table 3.2).

Table 3.1*: The mean and standard error of coherency, energy, and entropy of the healthy, lesion and border tissues at the epicenter and distant areas of the injury.*

	Coherency		Energy		Entropy	
	Epicenter	Distant	Epicenter	Distant	Epicenter	Distant
Healthy	0.26 (0.01)	0.27 (0.05)	98.5 (15.0)	134.0 (15.3)	-125.0 (20.0)	-109.0 (21.2)
Lesion	0.14 (0.05)	0.07 (0.01)	37.4 (3.4)	48.6 (6.7)	-30.0 (5.1)	-34.5 (7.9)
Border	0.14 (0.01)	0.16 (0.02)	77.4 (15.0)	129 (17.0)	-82.0 (13.2)	-96.0 (20.4)

3.4.4 No Difference Was Identified Between Locations of the Same Tissue Type

Analysis of paired images within mice did not show any differences between the epicenter and distant sites of the injury in lesions or the border tissue, after accounting for the variance within and across images. The lesion and border data were normalized with the mean outcome of the healthy tissue within individual images. Specifically, in epicenter and distant areas, the normalized mean ± standard error of coherency was 0.54 ± 0.06 versus 0.66 ± 0.04 in lesions and 0.38 ± 0.08 versus 0.39 ± 0.04 in the border tissue, and the normalized energy was 0.51 ±0.04

versus 0.58 ±0.05 in lesions and 0.49 ± 0.09 versus 0.36 ± 0.07 in the border. Finally, the normalized entropy was 0.82 ± 0.14 versus 0.64 ± 0.08 in lesions and 0.86 ± 0.18 versus 0.97 ± 0.24 in the border tissue (Figure 3.5).

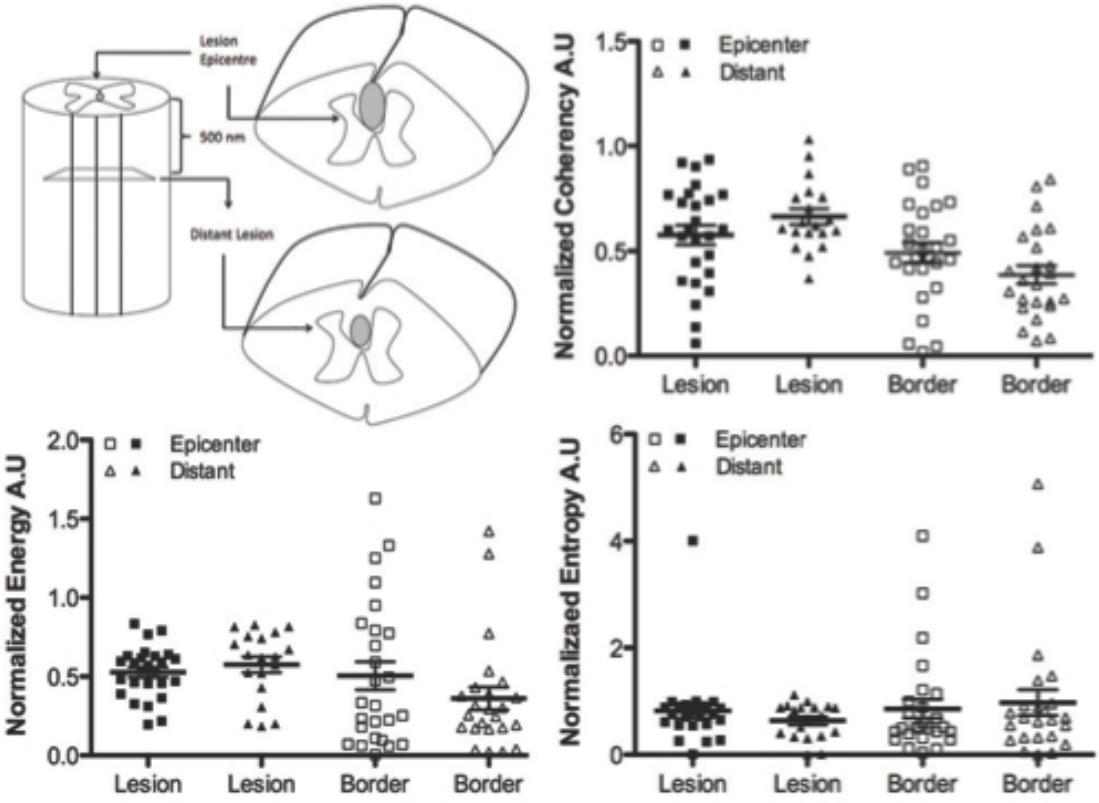

Figure 3.5- *Scatter plots of orientation outcomes at the epicenter and distant areas of the injury (cartoon in A). Shown in plots are normalized data by the mean outcome of the healthy tissue within individual images.*

3.5 Discussion and Summary

Based on quantitative analysis of structure tensor-based outcome measures in stained, standard histology images of the dorsal column of the mice spinal cord, I demonstrated that the myelin-

related integrity of white matter nerve fiber microstructure could be evaluated. I used the images from the lysolecithin model of demyelination and discovered that completely demyelinated lesions in the dorsal column had lower coherency and energy but higher angular entropy compared to the myelinated white matter tissue. After accounting for multiple comparisons, I found significant differences between the coherency of healthy and partially demyelinated white matter, which suggested the sensitivity of structure tensor analysis to myelin-related directionality.

After considering all images, I detected better tissue alignment in areas of greater myelin content compared to areas of less myelin. This is illustrated by the coherency outcome that decreased from the healthy, myelinated tissue to the border tissue with partial myelin presence and then to lesions, which lacked any myelin. The coherency index of structure tensor measures how similar the orientated structures are and is normalized to a range of 0 to 1. A coherency value of zero corresponds to an isotropic tissue with little uniform directionality whereas a value of 1 corresponds to a 1-directional structure (11). In these samples, healthy white matter nerve fibers were mostly oriented in a similar direction, corresponding to the highest coherency. This was expected as high directional homogeneity is observed in intact tissues. Conversely, injured nerve fibers with complete damaged myelin illustrated a minimal level of tissue alignment, which not surprisingly led to the greatest tissue heterogeneity, as shown by reduced energy and increased angular entropy. Collectively, the result of this analysis is in line with our current understanding of damaged neuronal environments, which showed that structure tensor-based outcome measure could detect distinct tissue directionality and distinguish tissues with different myelin states.

Structure tensor-based outcome measures were used to study the structural integrity of different tissue types based on their proximity to the lesion epicenter to evaluate different micro-environments. The coherency measure suggested that the healthy tissue continued to sustain its inherent well-oriented structures, regardless of its proximity to the lesion centre. The partially demyelinated border tissue followed the expected trend and contained less coherent structures compared to the healthy tissue. Consistent with these results, the demyelinated lesions sustained the worse outcome in both injury locations. Similarly at each site, the demyelinated areas were significantly disorganized compared to the healthy and border tissues, as shown by decreased energy and increased entropy. These measures however were not different between healthy and border white matter in either location. In this aim, I computed the degree of angular dispersion in structure directions to represent tissue entropy, instead of calculating the heterogeneity of image signal intensity, which enhanced the sensitivity of our orientation measures. The lack of difference between normal and partially demyelinated white matter may be explained by the large variance between border ROIs; which is in part due to presence of varying levels of myelin activity. Alternatively, this may also suggest the greater sensitivity of coherency than other measures of tissue microstructure.

To quantitatively evaluate the difference in structure organization between different sites of the injury, I normalized the coherency, energy, and entropy of lesion and border tissues by that of healthy tissues for each image. The results suggested that the lesion tissue contained more isotropic structures as per coherency analysis. By direct comparison to the healthy tissue, I found that there was no significant difference between the coherency, energy and entropy of different lesion locations and that both locations have equally damaged microenvironment. Specifically, to

evaluate whether myelin integrity differs between the epicenter and distant areas of the injury, I compared structure tensor measures in mice with paired images and did not identify differences between sites in any tissue. Growing evidence in the literature shows that remyelination typically begins at the boundary of demyelinated lesions in MS, raising the suspicion of distinct demyelination activities at different lesion locations (136). Through direct comparison in this study, I found that tissue regularity was similar between central and distant areas of demyelination, and this is consistent with findings in humans showing that various demyelination pathways converge in the late stages of MS, showcasing the ability of these directional measures (137).

My results support the use of advanced image analysis strategies such as structure tensor analysis to determine tissue integrity and anisotropy. In the literature, capturing consecutive high-resolution histology images using confocal microscopy is often used to evaluate tissue coherency, but this method is often limited to a small area ex vivo (138-141). In contrary to the limited converge of histological imaging, DTI is used to detect in vivo tissue anisotropy and has shown promising results (142, 143). Nonetheless, DTI is not specific to tissue pathology such as myelin. Moreover, recent evidence demonstrates the enhanced power of mathematical modeling of nerve fiber orientations in diffusion MRI compared to DTI, supporting the use of image analysis approaches (144). Indeed, the potential of structure tensor analysis has been shown in several studies focused on assessing the alignment of tissue microstructure, ranging from nerve fibers to elastin and collagen fibers in animals (10-12, 133).

In a similar image processing fashion, data analysis based on spatial frequency has also

demonstrated promising results. A very recent study explored the use of FT-based approach to evaluate the degree of myelination in longitudinal microscopic images of experimental autoimmune encephalomyelitis, another model of MS (108). Similar to using structure tensor analysis, the authors utilized the geometry of the ellipse, an indicator of tissue directionality, in the Fourier transformed images to compute a quantitative outcome for evaluation of myelin-related tissue organization. They discovered that the 2D FT approach had the potential to evaluate the orientation and directional anisotropy of myelinated axons.

This was a preliminary study that aimed to test the feasibility of structure tensor analysis as a measure of myelin integrity using standard histological images. The small sample size was a major limitation. Another limitation was that the ROIs were selected from tissues with optimal staining intensity based mostly on visual perception. This may have led to a higher variance between samples, particularly in the border tissue. To address the issue, I used fixed ROI sizes across tissue types and verified the robustness of structure tensor measures to ROI size, normalization, and relative location before starting the analysis. Furthermore, I assessed the directional properties of tissue structure based only on myelin staining. Further work is needed to evaluate the impact of axonal damage on directional properties of lesion tissue.

Overall, in this aim, I found that tissue anisotropy could be altered by the myelin integrity in white matter. This provided proof-of-principle evidence that changes in myelin content may lead to alterations in the coherency and complexity of tissue structure that can be assessed using structure tensor analysis. As MR images are the biophysical translation of in vivo tissue property, these findings may suggest that structure tensor analysis is applicable to the MR images in the

future. If successful, this should improve our ability to monitor disease development, and in assessing the potential of new medicines for patients with demyelinating diseases including but not limited to MS.

Chapter Four: **Evaluation of the Impact of Interpolation Techniques and Image Size on Structure Tensor Analysis Using Standard MRI**

4.1 Introduction

Given that structure tensor analysis has demonstrated strong evidence for its potential to evaluate myelin integrity in LFB-stained histological images in Chapter 3, I aimed to investigate whether it is feasible to use this method in MR images in vivo. Particularly, I seek to test the robustness of structure tensor analysis to the change in image matrix size and to the use of different interpolation techniques, before using it to measure pathology. Interpolation is an image processing technique commonly used to adjust image size and resolution to improve quality or facilitate comparison of medical images obtained under different conditions (145). As conventional MRI is routinely used in the diagnosis and management of MS (146), my goal is to validate the technical feasibility of using structure tensor analysis in one of the conventional MRI contrasts, the T_2-weighted MRI.

In this aim, I evaluated the robustness of structure tensor-based outcomes to commonly used interpolation techniques, namely bilinear, bicubic, and basis spline (b-spline) methods (147, 148). I also evaluated the impact of these techniques on each index of structure tensor analysis used in this thesis using MR images with different matrix sizes. Finally, I investigated the impact of interpolation on eigenvectors and eigenvalues that were used to derive the outcomes in structure tensor analysis.

4.2 Image Interpolation

Interpolation is a common and at times a necessary process that aims to approximate a new set of

unknown data from an available source with little artefact and distortions (149). In image processing, different interpolation methods relate to different mathematical algorithms that are used to estimate the unknown pixel, leading to the reconstruction of an image with altered spatial resolution through up- or down-sampling (150). Interpolation has applications in many areas of engineering, physics (151, 152) and computer science (153), beyond image processing.

In MRI studies, one of the most common applications of interpolation is in the co- registration field, mostly for images obtained at different time points or from different scanners (154, 155). In this procedure, image interpolation is needed to estimate the intensity value of each voxel in a target image to match that in the source image for spatial alignment. This will allow for pooling and comparison of data as well as detection of patterns that are due to structural or pathological differences (156). Thus, it is essential to determine how structure tensor-based measures change with different interpolation methods for improved interpretation of results in future applications. In the next section, I have reviewed 3 commonly used interpolation methods in MR imaging.

4.2.1 Bilinear Interpolation

Bilinear interpolation is one of the most basic methods of approximation. Bilinear interpolation of unknown data sets (pixel intensities) in an image is carried out in two directions using the intensities of the four neighbouring pixels (figure 4.1) (157). Bilinear interpolation is based on linear first-degree polynomials, which are mathematical equations that use variables (x, y, z) and coefficients to describe data or characteristics in 1, 2 or 3 dimensional grid. Due to its lower degree of flexibility to create continuous data, bilinear method has a lower degree of accuracy than bicubic and basis spline methods and thus is more likely to create distortions in the

interpolated image (148). The use of bilinear interpolation results in jagged edges (non-smooth line) on image lines and also loss of high frequencies, leading to strong blurring of images (158). The biggest advantage of bilinear interpolation is its short computation time.

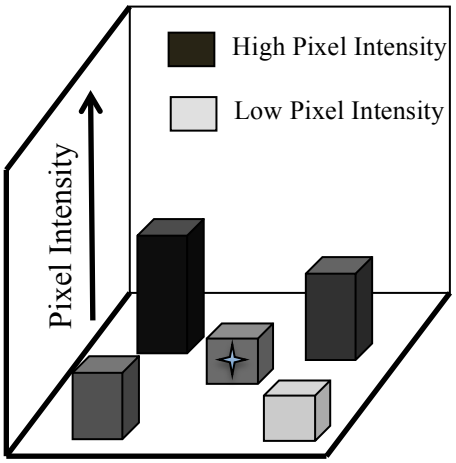

Figure 4.1- *A simplified schematic of bilinear interpolation method showing a general approach for approximation of an unknown pixel intensity value (box with the star). Four neighbouring pixels with known intensities are used for the approximation. The legend depicts the color-coded intensity map.*

4.2.2 Bicubic Interpolation

Bicubic or convolution interpolation is the estimation of unknown data points using the cubic interpolation method in 2 dimensions using the surrounding 4x4 pixels as the source of estimation (157). In this process, known pixel intensities are given specific weighing power based on their proximity to the pixel that needs to be estimated. The bicubic interpolation is a third degree piecewise polynomial function that creates a continuous data set from an original discrete data set (159). Polynomials are commonly used in interpolation techniques due to their simple mathematic-derived parameters and their ability to evaluate any continuous data with

specific endpoints. Nonetheless, higher degree polynomials are not always accurate (160). Therefore, piecewise polynomials are often used in which more than one polynomial functions are implemented to enhance accuracy, while keeping the degree of the polynomial function constant.

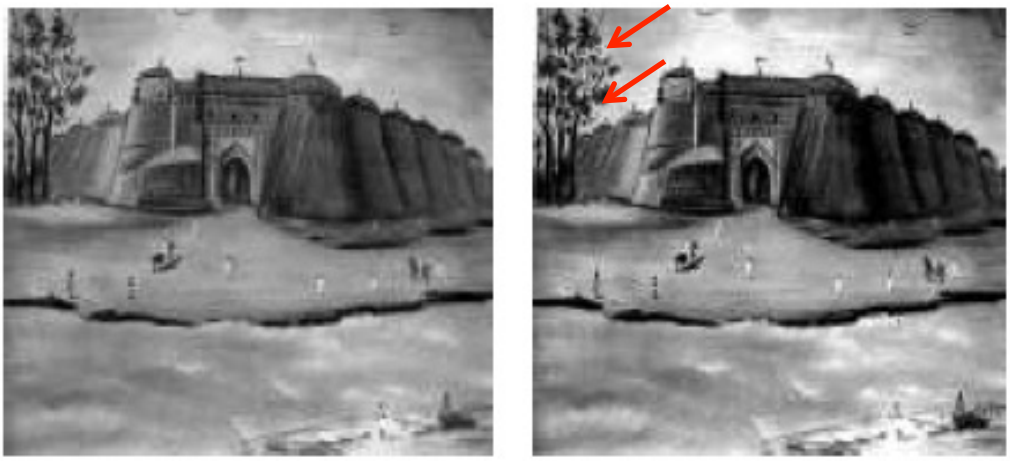

Figure 4.2- *An illustration of blocking artefact in a digital image. Panel A shows the original image and panel B shows the image with block-like projections: Red arrows point out the artefact in the tree branches. Image is obtained from Singh et al, Digital Signal Processing, 2007* (161).

The error associated with bicubic interpolation is smaller than that generated by the bilinear method (159). This is due to the inability of bilinear approach to reproduce more than one first-degree polynomial. The saw-like projections of edges are still detectable in images that are treated with bicubic interpolation but the impact is much less than using the bilinear method. Reducing image contrast is one of the disadvantages of bicubic interpolation (loss of sharp color differences that make image parts distinguishable), due to averaging of neighbouring pixel

values (157). In addition, this technique is computationally more expensive than the bilinear method and causes block-like distortion in images (figure 4.2).

4.2.3 Basis Spline Interpolation

Similar to bicubic interpolation, basis spline or b-spline interpolation belongs to a large mathematical family of functions known as piecewise polynomial functions (162). The term spline refers to a flexible string of material that can go through various points in space in a smooth manner (163). In computer-based systems, we use basis spline functions as a way to connect known experimental data while approximating the unknown data points between them. As previously described, polynomial functions are mathematical expressions of variables and coefficients that define the location of data points. Depending on the data source, the b-spline polynomial functions with n^{th} degree contain coefficients that could help approximate the target signal accurately.

B-spline is a continuous spline interpolation that can offer a more accurate approximation than the linear methods (164). This approach was first used in image processing by Hou and Andrews in 1978 (165). The degree of variables in b-spline interpolation is typically 3 since a degree of higher than 3 behaves like a normal polynomial and lacks the advantage of piecewise polynomials. These functions are commonly used in image resolution conversion and resizing of images. They are also used in zooming and visualization, geometric image transformation, image compression, and registration. The advantage of b-spline interpolation comes from its minimal aliasing property as compared to the bilinear method and its small error in the approximation of final pixel intensities(147). Using b-spline, it is also possible to have a continuous representation

of the data in 1 or more dimensions. These functions are less likely to oscillate than bicubic functions, generating interpolated pixel intensities with a smaller error, which leads to conservation of image edges. A minor disadvantage of this method is that it smoothens out data by reducing the excess noise more than needed (166).

4.3 Methods

4.3.1 Image and ROI Characteristics

I used T_2-weighted MR images to test the robustness of structure tensor-based measures. The coherency, energy, and angular entropy measurements were generated as previously described in chapter 3. A total of 15 ROIs were chosen from 5 axial MR images, acquired from the cervical spinal cord (C4/5) of a healthy C57B/6 mouse. ROIs were drawn at the dorsal column and grey matter areas of the spinal cord.

4.3.2 Image Interpolation

The original image with a matrix size of 256x256 was interpolated into 512x512 and 768x768 images using the bilinear and bicubic methods in ImageJ. An ImageJ plug-in named Resize was used for b-spline interpolation of the same images. To evaluate the impact of interpolation on images with the same size, 256x256 images were up-sampled to 512x512 and then down-sampled to 256x256 using the same three interpolation methods. I refer to this group of images as interpolated 256x256 images. ROIs of 11x11 pixels were utilized in both the original and interpolated images, sized 256x256. 22x22-pixel ROIs were used in the interpolated 512x512 images and 33x33-pixel ROIs in the 768x768 images. The same ROI location covering the same anatomical regions was used before and after interpolation. The ratio of the ROI to image sizes

was consistent in order to cover the same anatomical regions at all times, regardless of the matrix size. Overall, 15 ROIs were analyzed from each type of images: 256x256 (original), 256x256 (interpolated), 512x512 (interpolated), and 768x768 (interpolated).

4.3.3 Eigenvector and Eigenvalue Calculation

To evaluate the impact of interpolation on the eigenvector and eigenvalues of an image, I calculated the eigenvectors and eigenvalues of ROIs before interpolation and compared them to the post-interpolated eigenvectors and eigenvalues. The term eigen means critical characteristics in an object (167). The eigenvector of an image is the axis of transformation of primary vectors in an image where the vector describes the direction of information such as dominant orientation in an image. Every eigenvector has an eigenvalue, which describes the magnitude of the eigenvector. Upon transformation of an image, the eigenvector may not change but its eigenvalue could. Testing the impact of interpolation on eigenvectors and eigenvalues is essential as these image characteristics are the fundamental mathematical traits used in structure tensor analysis to evaluate tissue directions.

To calculate eigenvectors and eigenvalues, I used the same T_2-weighted MR images as described in the previous section. Twenty ROIs from 4 T_2-weighted MR images of were chosen from muscle bundles surrounding the vertebrae. ImageJ was used to measure the pixel intensity within each ROI. Recorded pixel intensities were then imported into an open source online calculator (Bluebit matrix calculator) to calculate the initial, estimated set of complex numbers (a+bi) corresponding to individual eigenvectors and eigenvalues of that ROI. These numbers were then

converted to the final single value of the matching eigenvalue "c", using the formula "$a^2+b^2=c^2$ ". Finally, Arc tan (b/a) was used to evaluate the eigenvector in radians.

4.4 Statistical Analysis

All analyses were conduced using Graphpad Prism version 5.0. Parametric 1 way ANOVA followed by post hoc Dunnett's multiple comparison test was used to compare groups before and after interpolation (control). Tukey's post hoc test was conducted to compare the outcome between different interpolation methods. Two-tailed Pearson correlation analysis was done to study the relationship between changes of variance in pixel intensity and eigenvalues. $p<0.05$ was deemed to be significant.

4.5 Results:

4.5.1 Coherency Was The Most Robust Measure To Interpolation

Based on the analysis of selected ROIs at 3 different image matrix sizes, I discovered that the coherency outcome from structure tensor analysis preserved the most consistency before and after image interpolation (Table 4.1). Specifically, I found no significant difference ($p=0.22$) between the coherency of original 256x256 images (mean ± standard error = 0.24± 0.03) and the coherency of bilinear-interpolated 256x256 (0.33±0.14), 512x512 (0.26± 0.03) and 768x768 images (0.27± 0.03). Post hoc Dunnett's multiple comparison test did not indicate a significant difference between the original and any of the interpolation groups ($p>0.05$). Similarly, there was no difference ($p = 0.83$ for ANOVA and $p > 0.05$ for post hoc Dunnett's test) between the coherency of the original and interpolated images based on the bicubic technique: 256x256 (0.29 ± 0.13), 512x512 (0.25±0.03) and 768x768 images (0.25±0.03), or based on the b-spline

technique: 256x256 (0.24±0.10), 512x512 (0.24± 0.03) and 768x768 images (0.23± 0.03), where p = 0.99 for ANOVA and p > 0.05 for post hoc Dunnett's test.

Table 4.1- *Mean and standard error of coherency measure before and after image interpolation. A total of three different methods were tested. P values were obtained based on one-way ANOVA. Post hoc Dunnett's multiple comparison test was done to compare the before- and after-interpolation groups.*

Method	Before	After			p (ANOVA)	p (Dunnett's)
	256	256	512	768		
Bilinear	0.24 ± 0.03	0.33 ± 0.14	0.26 ± 0.03	0.27 ± 0.03	0.22	>0.05
Bicubic	0.24 ± 0.03	0.29 ± 0.13	0.25 ± 0.03	0.25 ± 0.03	0.83	>0.05
B-spline	0.24 ± 0.03	0.24 ± 0.10	0.24 ± 0.03	0.23 ± 0.03	0.99	>0.05

4.5.2 Both The Energy and Angular Entropy Measures Changed After Interpolation

Based on the analysis of the same ROIs, I showed that the energy and angular entropy measures were not as robust as coherency to interpolation (tables 4.2-4.3). I found a significant difference ($p<0.0001$) between the energy of original 256x256 images (307557± 14014) and the energy of bilinear-interpolated 256x256 (167046± 29844), 512x512 (103078± 7372) and 768x768 images (36608± 1957). Post hoc Dunnett's multiple comparison indicated a significant difference between the before- and after- interpolation groups ($p<0.05$). Similarly, comparison of energy for the original and bicubic-interpolated 256x256 (225176 ± 40724), 512x512 (111356± 6892) and 768x768 images (50914± 3730) indicated a difference between groups ($p<0.0001$). Consistent with this observation, post hoc Dunnett's multiple comparison test indicated significant

difference between the before- and after- interpolation groups ($p<0.05$). In a similar trend, I found a significant difference ($p<0.0001$) between the energy of original 256x256 images and the energy of b-spline-interpolated 512x512 (115392± 6150) and 768x768 images (51992± 2466), and Dunnett's test again indicated a significant difference between the energy of before- and after- interpolation images ($p<0.05$)

Table 4.2- *Mean and standard error of energy measure before and after image interpolation. A total of three different methods were tested. P values were obtained based on one-way ANOVA. Post hoc Dunnett's multiple comparison test was done to compare the before- and after-interpolation groups.*

Method	Before	After			p (ANOVA)	p (Dunnett's)
	256	256	512	768		
Bilinear	307557 ±14014	167046 ±29844	103078 ±7372	36608 ±1957	<0.0001	<0.05
Bicubic	307557 ±14014	225176 ±40724	111356 ±6892	50914 ±3730	<0.0001	<0.05
B-spline	307557 ±14014	292395 ±51736	115392 ±6150	51992 ±2466	<0.0001	<0.05

Note: no significant difference (P>0.05) between 256x256 b-spline-interpolated image and the before-interpolated image based on Dunnett's Multiple Comparison Test

Similarly to measures of energy, I also found a significant difference ($p<0.0001$) between the entropy of original 256x256 images (-37 ± 6.4) and the entropy of bilinear-interpolated 256x256 (-43± 20.5), 512x512 (-252± 29.8) and 768x768 images (-789± 49.5). Post hoc Dunnet's multiple comparison indicated a significant difference between the before- and after-interpolation groups ($P<0.05$). Likewise, comparison of energy for the original and bicubic-interpolated 256x256 (-41± 22.2), 512x512 (-252± 29.8), and 768x768 images (-789± 49.5)

indicated a difference between groups ($p<0.0001$). Post hoc Dunnet's multiple comparison test indicated significant differences between the before- and after- interpolation groups ($p<0.05$). In a similar trend, I found a significant difference ($p<0.0001$) between the entropy of original 256x256 images and the entropy of b-spline-interpolated 512x512 (-236± 26.9), and 768x768 images (-695± 53.2). Dunnet's test indicated a significant difference between the entropy of before- and after- interpolation images ($p<0.05$).

Table 4.3- *Mean and standard error of entropy measure before and after image interpolation. A total of three different methods were tested. P values were obtained based on one-way ANOVA. Post hoc Dunnett's multiple comparison test was done to compare the before- and after-interpolation groups*

Method	Before	After			p (ANOVA)	p (Dunnett's)
	256	256	512	768		
Bilinear	-37 ± 6.4	-43 ± 20.5	-252 ± 29.8	-789 ± 49.5	<0.0001	<0.05
Bicubic	-37 ± 6.4	-41 ± 22.2	-232 ± 27.4	-540 ± 122.4	<0.0001	<0.05
B-spline	-37 ± 6.4	-34 ± 21.7	-236 ± 26.9	-695 ± 53.2	<0.0001	<0.05

Note: no significant difference ($P>0.05$) between 256x256-b spline-interpolated images and the before-interpolated image based on Dunnett's Multiple Comparison Test

Normalization of interpolated structure tensor values with the mean of the values from original 256x256 images indicated a smaller change for the coherency at higher matrix sizes, post-interpolation (figure 4.2-4.4). I found a significant difference ($p<0.0001$) between the normalized coherency, energy and entropy of bilinear-interpolated 512x512 and 768x768 images (figure 4.2). Tukey's post hoc test indicted significant differences between all measures at both

image matrix sizes. The coherency (0.44± 0.09) and energy (0.63± 0.03) measures were less impacted compare to entropy (5.88± 0.81) at 512x512 pixels. Similarly, the coherency (0.49± 0.08) and energy (0.88± 0.01) measures were also less impacted compare to entropy (20.43± 1.60) in 768x768 interpolated-images. Interestingly, despite its higher degree of change before and after interpolation, the normalized energy values were more clustered together across all samples. Moreover, the entropy measure had the highest normalized change and a larger distribution compare to the other measures.

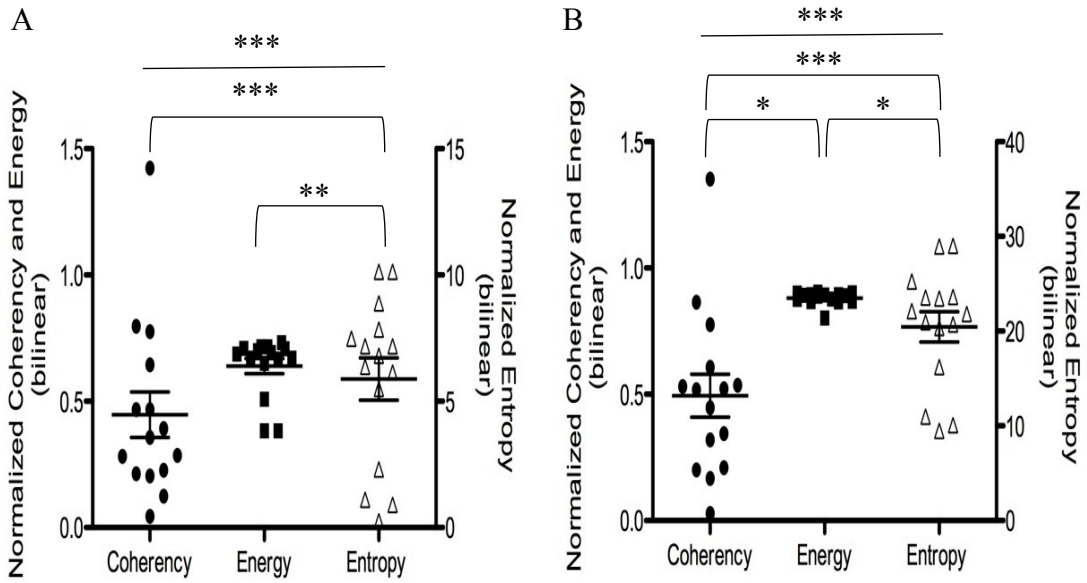

Figure 4.3- *Normalized scatter plots of coherency, energy and entropy measures obtained after bilinear interpolation for 512x512 (panel A) and 768x768 images (Panel B). The mean of the original measurements per image was used as the reference for the normalization. One-way ANOVA followed by Tukey's post hoc test was performed.*

In a similar trend, I found a significant difference ($p<0.0001$) between the normalized coherency, energy and entropy of bicubic-interpolated 512x512 and 768x768 images (figure 4.4). The

coherency (0.41± 0.08) and energy (0.63± 0.02) measures were less impacted compared to entropy (5.76± 0.78) at 512x512 pixels. Similarly, the coherency (0.38± 0.09) and energy (0.83± 0.01) measures were also less impacted compare to entropy (16.93± 2.1) in 768x768 interpolated-images.

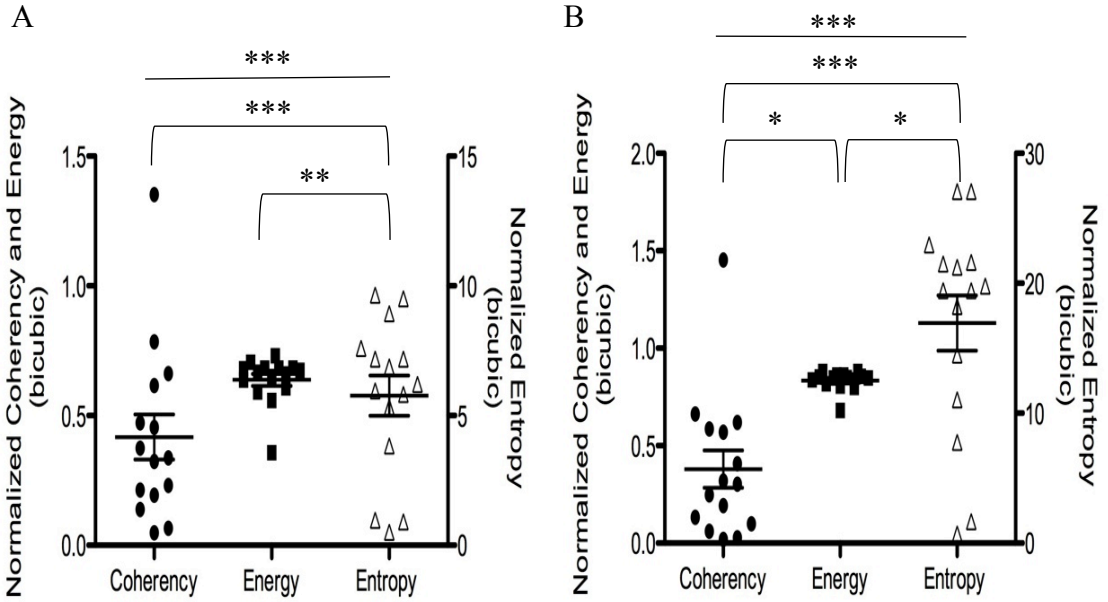

Figure 4.4- *Normalized scatter plots of coherency, energy and entropy measures obtained after bicubic interpolation for 512x512 (panel A) and 768x768 images (Panel B). The mean of the original measurements per image was used as the reference for the normalization. One-way ANOVA followed by Tukey's post hoc test was performed.*

The normalized coherency, energy and entropy of b-spline-interpolated 512x512 and 768x768 images were also significantly different ($p<0.0001$) (figure 4.4). The coherency (0.37± 0.07) and energy (0.69± 0.44) measures were less impacted compare to entropy (5.44± 0.73) at 512x512

pixels. Similarly, the coherency (0.34± 0.07) and energy (0.83± 0.01) measures were also less impacted compare to entropy (17.97± 1.5) in 768x768 interpolated-images.

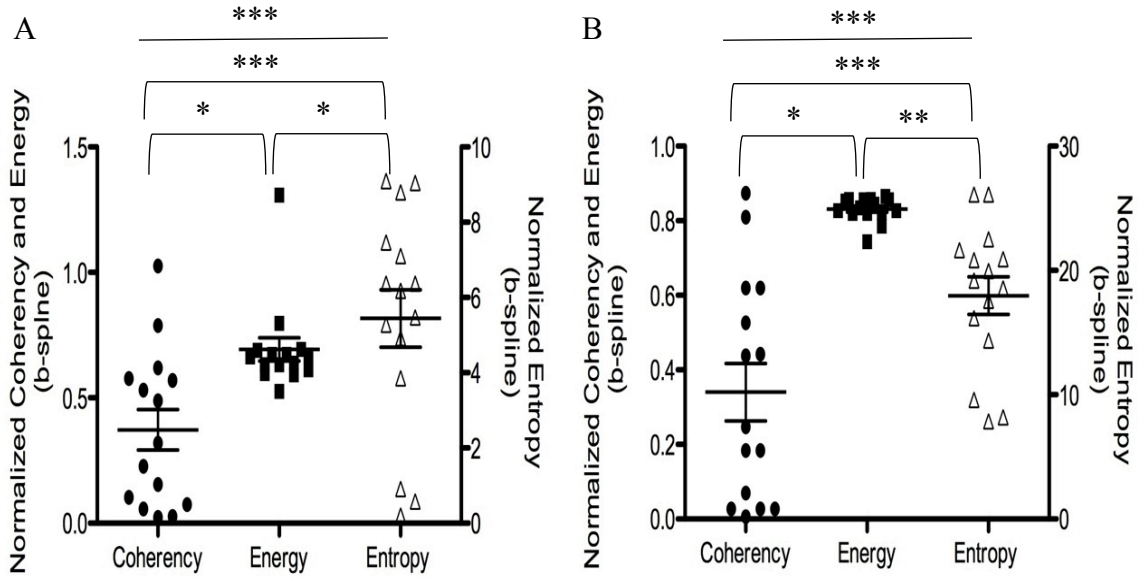

Figure 4.5- *Normalized scatter plots of coherency, energy and entropy measures obtained after the b-spline interpolations for 512x512 (panel A) and 768x768 images (Panel B). The mean of the original measurements per image was used as the reference for the normalization. One-way ANOVA followed by Tukey's post hoc test was performed.*

4.5.3 Basis Spline Method Is the Most Reliable Method of Interpolation

Based on the evaluation of normalized bilinear-, bicubic- and b-spline - interpolated 256x256 images, b-spline was the most reliable method (figure 4.5). The values obtained from the ROIs of interpolated images were normalized with the mean of the same ROIs at the original matrix size. One-way ANOVA followed by Tukey's test was used to compare the normalized coherency, energy, and entropy of 256x 256 interpolated images using bilinear, bicubic, and b-spline methods. The difference was significant for energy and entropy measures ($p<0.0001$), but not for

coherency. I also found that the b-spline method produced the smallest degree of change for all outcomes after interpolation. In particular, based on quantification of normalized outcome measures, b-spline-interpolated images had significantly ($p<0.0001$) smaller change in energy (0.14 ± 0.02) and entropy (0.49 ± 0.88) than the bilinear-interpolated images (energy=0.45 ± 0.02, entropy=1.17 ± 0.15). Specifically for the energy measure, the normalized value after b-spline interpolation (0.14 ± 0.02) was significantly smaller ($p<0.05$) than the value obtained by the bicubic method (0.26 ± 0.03). No significant differences were noted between the methods in the evaluation of coherency, as this measure was deemed to be the most robust to interpolation based on previous analyses ($p>0.05$).

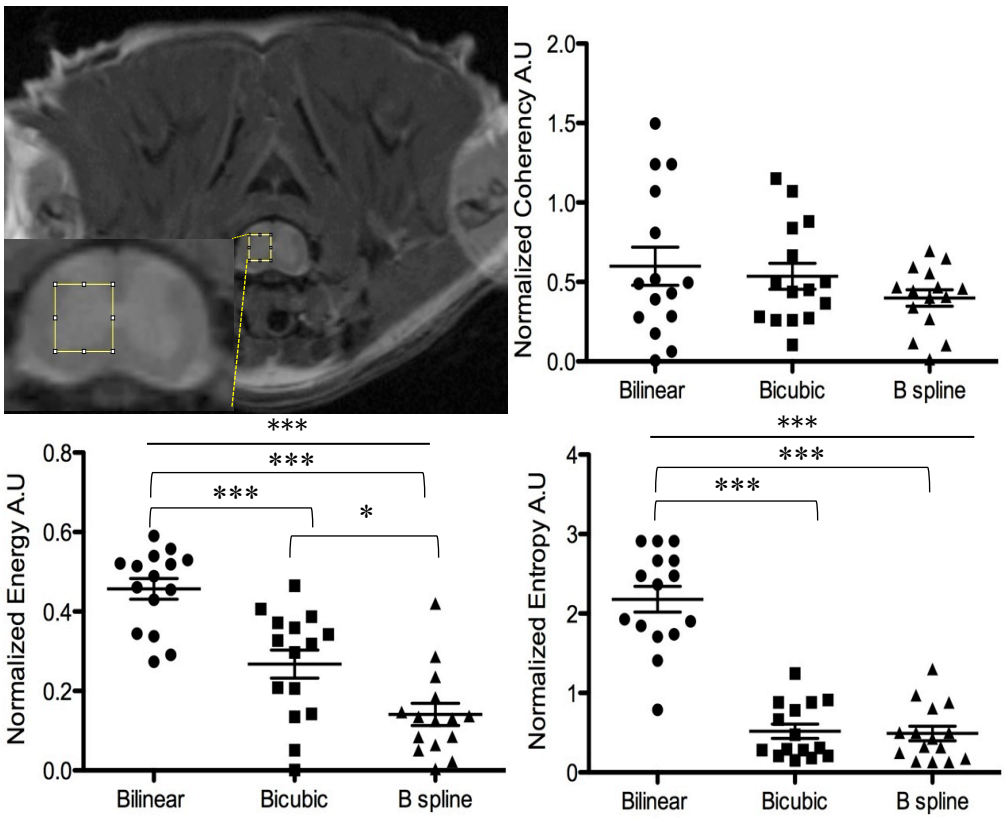

Figure 4.6- *Axial MR image of the cervical region of a mouse spinal cord, showing a sample ROI. The plots show the results of different interpolation methods for different outcome measures*

in interpolated 256x256 images through normalized measurements. Values from original 256x256 images were used as the reference for the normalization. One-way ANOVA followed by Tukey's post hoc test was performed.

4.5.4 Basis Spline Has Less Impact on Eigenvalue and Pixel Intensities Than Bilinear and Bicubic Interpolations

Unlike the bicubic and bilinear methods, b-spline interpolations had less impact on the eigenvalues of interpolated images (figure 4.6 A). One-way ANOVA analysis of the eigenvalues of interpolated 256x256 images was found to be significant ($p<0.0001$). The original eigenvalues (4.97± 0.05) changed after bilinear interpolation (4.82±0.07), although a larger spread in bilinear-interpolated eigenvalues is evident comparing to the original. The original eigenvalues changed significantly ($p<0.001$) after bicubic interpolation (4.69±0.04) while eigenvalues of b-spline interpolated-images (4.98±0.06) were not significantly impacted. Furthermore, the normalization of interpolated eigenvalues with the original showed smaller changes for b-spline-interpolated images than bilinear-interpolated images ($p<0.001$) (figure 4.3 B). Consistent with these results, normalized eigenvalues of bicubic-interpolated images were smaller than those of bilinear-interpolated images ($p<0.001$). Consistent with the result of eigenvalue alterations after interpolation, the standard deviation and peak of image histogram also changed after bilinear and bicubic interpolations (figure 4.7). However, b-spline interpolation did not impact the standard deviation of pixel intensities. The peak of image histogram after b-spline interpolation also remained similar to the original.

Contrary to the result of eigenvalue analyses, interpolation of the original images did not have a significant impact on image eigenvectors ($p>0.05$) (figure 4.3 C). The degree of global change (sum of changes from median) was calculated for all eigenvectors after interpolation. The median of the eigenvectors, which was consistently zero among all samples, was used as a reference for this calculation. The degree of global change for original images (5.55±0.35) was negligible after bilinear (6.09±0.37) and bicubic (5.67± 0.44) and b-spline (5.90±0.29) interpolations ($p>0.05$).

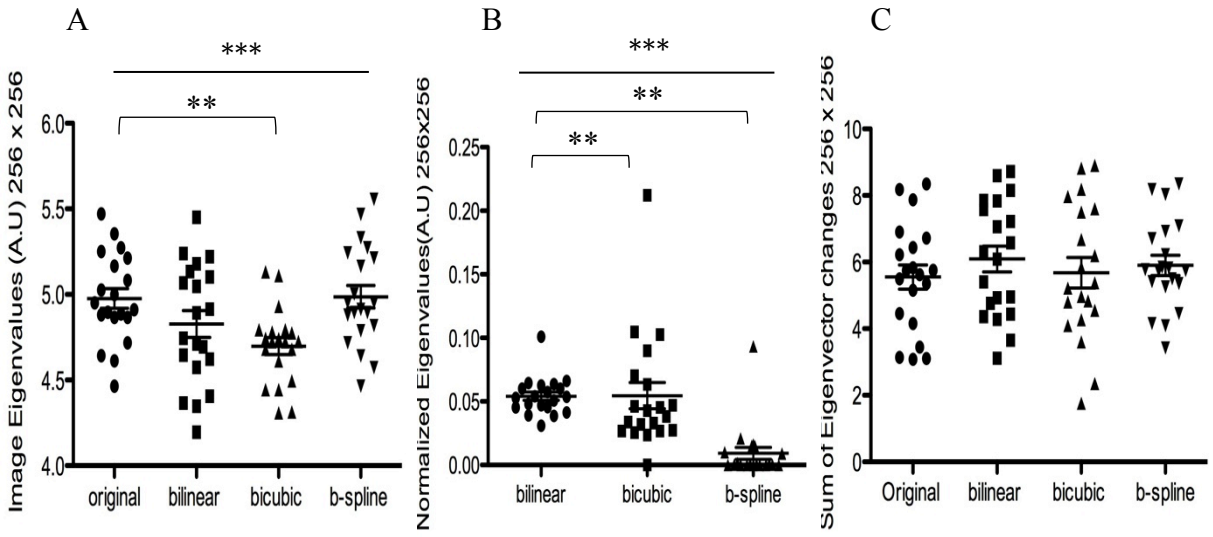

Figure 4.7- *Scatter plots of ROI mean eigenvectors and eigenvalues before and after interpolation of 256x256 images. Panel A shows the mean and standard error of eigenvalues for 20 ROIs (one-way ANOVA and Dunnett's post hoc test). Panel B shows the normalized eigenvalues based on the original measurements and compares the impact of different methods on eigenvalues (Tukey's test). Panel C shows the impact of interpolation on the range of eigenvectors before and after interpolation.*

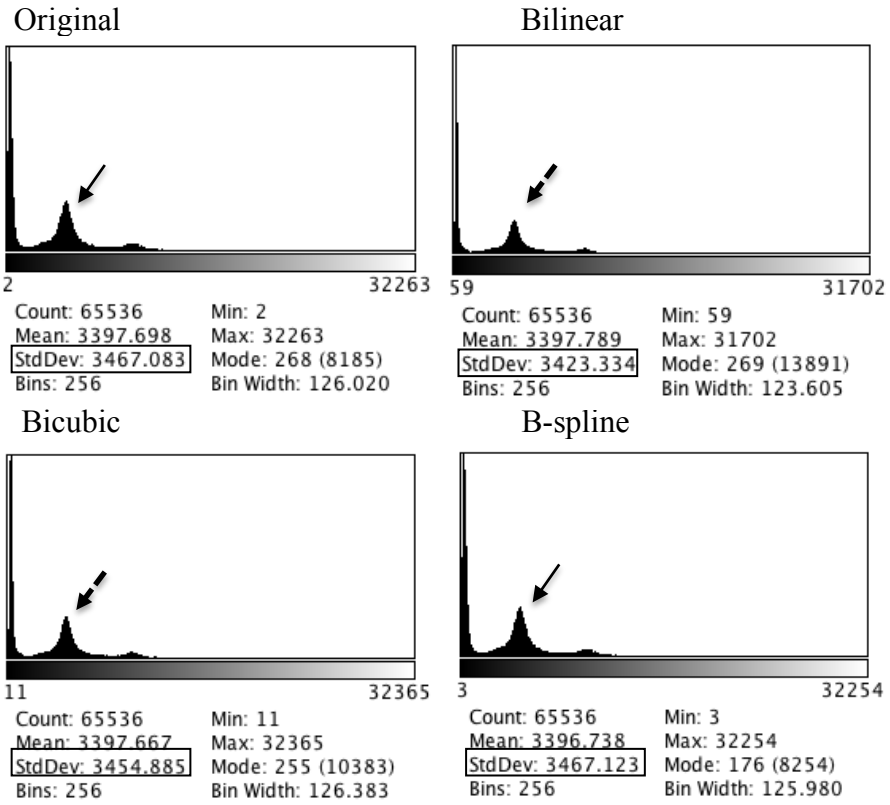

Figure 4.8- *Histogram of pixel intensity distributions in original and interpolated 256x256 images. The standard deviations of pixel intensities are highlighted before (A) and after interpolation (B-D). Standard deviation of pixel intensities in b-spline interpolated images mimics that of the original. The peak of image histogram changed after bilinear and bicubic interpolations (dashed arrows). Solid arrows point out similar histogram peaks for the original and b-spline interpolated images.*

4.5.5 Eigenvalues Are Robust to Change of Variance in Pixel Intensities

In order to better understand the impact of image interpolation on images, I investigated the impact of changes in the variance of pixel intensities on eigenvalues of ROIs. Based on visual observation of raw data for each ROI, there appeared to be a positive relationship between the variance of pixel intensities and eigenvalues. However, no significant correlation was detected

based on quantitative analysis. After b-spline interpolation, the correlation coefficient between the eigenvalue and variance of pixel intensities was 0.01 for 256x256 and 0.14 for 512x512 images. This was consistently smaller than the coefficients calculated for bicubic-interpolated (R=0.06 for 256x256 and R=0.16 for 512x512) and bilinear-interpolated images (R=0.3 for 256x256 and R=0.23 for 512x512).

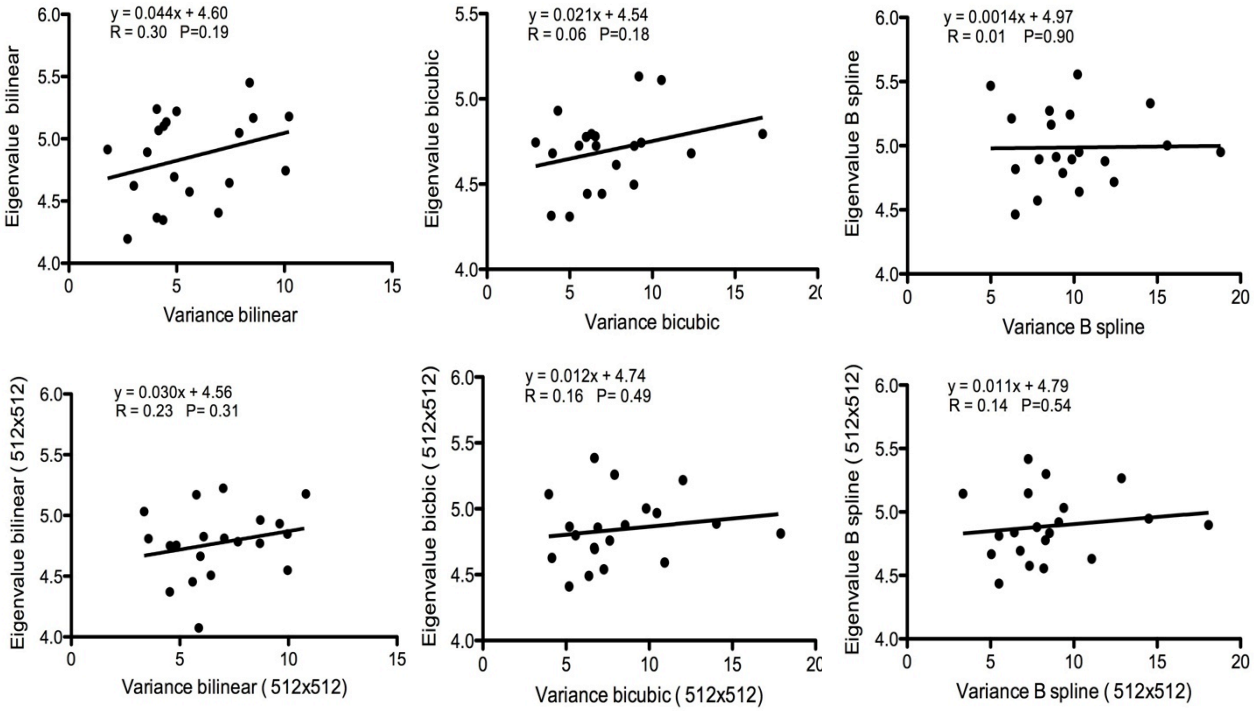

Figure 4.9- *Correlation plots of eigenvalues and pixel intensity variances of 20 ROIs after bilinear, bicubic and b-spline interpolation for 256x256 images (top) and 512x 512 images (bottom). No significant correlation between pixel intensity variance and eigenvalues were noted ($p>0.05$).*

4.6 Discussion and Summary

Using standard T_2-weighted images, I evaluated the robustness of structure tensor-based measures and their reliability to a commonly used image-processing tool known as image interpolation. Specifically, I showed that the coherency outcome is the most robust to image interpolation as before- and after- interpolation measurements were consistently similar. However, the after-interpolation energy and angular entropy measurements were significantly different from the original. I also showed that b-spline is the most reliable method of interpolation as the generated measurements in b-spline-interpolated images mirrored those of the original images. To achieve a broader perspective on the global effect of interpolation and its potential manipulation on mathematical characteristics of MR images, I studied the impact of interpolation on eigenvectors and eigenvalues and determined the b-spline method to have less impact on eigenvalues. This was followed by a non-significant correlation analysis, illustrating the robustness of eigenvalues to changes of variance in pixel intensity.

Comparison of coherency of ROIs of original 256x256 image to the ROIs of the interpolated 512x512 and 768x768 images illustrated a lower degree of manipulation for this outcome compared to the energy and entropy, regardless of the interpolation method used. Consistent with these results, the normalized changes observed in the energy and entropy outcomes were consistently higher than the original. With regards to more negative angular entropy changes after interpolation, one can postulate that approximation of unknown pixel values based on known data could result in a smoother image where the degree of disorder or signal heterogeneity is lowered. A consistent decrease in energy measurements after interpolation was also noted. To date, the mechanisms of energy calculation are not fully understood but I

speculate that a decrease in energy measurements after interpolation is possibly due to a decrease in eigenvalues. Based on mathematical computation of energy, the sum of eigenvalues from the dominant and minimal eigenvectors in the ROI determines the degree of tissue directional organization. A decrease in eigenvalues would lead to a smaller eigenvalue-sum and a reduced energy measurement, which is in line with my observation of energy alterations. Due to the preliminary nature of this study, further verification is needed to explore the mechanisms of outcome changes post-interpolation.

After comparison of original and interpolated 256x256 images, the b-spline approach was deemed to be the most reliable method of interpolation for analysis of MR images by structure tensor analysis. In particular, this approach generated significantly better evaluations in energy and angular entropy outcomes. Due to the established robustness of the coherency to interpolation, coherency values generated by different interpolation methods experienced little deviation from the original; thus all interpolation methods appear to be suitable for evaluation of coherency. Specifically, comparison of different interpolation methods illustrated the superiority of b-spline approach based on its ability to generate measurements with little deviation from the original. The bicubic method was the second most reliable method of interpolation as it generated values that resembled those of the original with a higher degree of deviation than b-spline. Furthermore, the bilinear method was the least reliable due to its inability to generate consistent measurements upon interpolation. These results are consistent with previous studies that recognized b-spline interpolation as a superior approach to bilinear and bicubic, due to its minimal degree of error upon interpolation (168). The superiority of the b-spline technique is

largely due to its higher degree of flexibility and smoother polynomial that can fit a larger number of data set in a 3D space (169).

In order to have a global picture of the impact of different interpolation methods on images, I studied the impact of interpolation on eigenvectors and eigenvalues of original 256x256. Based on the analysis, the distribution and mean of eigenvalues obtained after b-spline interpolation closely matched that of the original in 256x256 images, where no significant difference was present between the two groups. The bicubic method had a relatively large impact on the eigenvalues as the mean of the values significantly declined after interpolation in 256x256 images. The bilinear interpolation method caused a larger spread in image eigenvalues compared to the original than the other methods. Consistent with my previous results, I did not find any significant differences between eigenvalues of the original image and b-spline interpolated images sized at 256x256 pixels. The effect of interpolation on eigenvalues is crucial as image eigenvalues are critical to the computation of most outcome measures generated by structure tensor analysis. Further comparison of different interpolated methods in light of eigenvalues illustrated the ability of b-spline to preserve the image eigenvalues post interpolation, a characteristic that the bicubic and bilinear method significantly lacked. Comparison of original image histograms and pixel intensity deviations to post-interpolation results further showed the reliability and negligible impact of b-spline on images. To evaluate the impact of interpolation on eigenvectors, I calculated the eigenvectors of the 11x11 ROIs from the original and interpolated images. Similar to the eigenvalue distribution, the distribution and mean of sum of changes in eigenvectors with reference to the median value in b-spline-treated 256x256 images

closely resembled that of the original image. Nonetheless, image interpolation did not significantly affect the eigenvectors of 256x256 images.

Through a correlation analysis, I did not find any significant relationship between the eigenvalue of the images and the changes in the variance of pixel intensities. Based on an initial observation of raw data, decreases in the intensity variance in addition to changes in eigenvalues seemed to exist after interpolation. However, it was evident that image eigenvalues were robust to changes of variance in pixel intensity. This is encouraging as interpolation methods are performed to achieve a desired set of new image data with little to no artefacts. Although no significant changes were observed, utilization of different types of image interpolation method altered the correlation coefficients.

In summary, I provided technical validation means for utilization of structure tensor based-measures in standard MR images. Although this was a small study that explored the impact of interpolation on 35 ROIs, the results were consistently significant and were in line with previous research. Specifically, I showed that the coherency measure is the most robust to image interpolation. The results also showed that the choice of interpolation impacts the degree of change in structure tensor measurements through which b-spline was deemed to be the most reliable. Based on these results, it is clear that bilinear and bicubic methods may not be used for structure tensor analysis of MR images. The impact of interpolation on image eigenvectors and eigenvalues was explored, illustrating the significant change that interpolation could have on eigenvalues. Unlike other methods, the b-spline approach had a minimal effect on eigenvalue of interpolated images.

Chapter Five: **Assessing the Potential of Structure tensor Analysis to Measure De- and Re-myelination in T_2-weighted MRI of Mouse Spinal Cords**

5.1 Introduction

Conventional MR imaging is used as a standard tool in the diagnosis and management of MS in clinical practice. In clinical trials, it is also used to evaluate the safety and efficacy of candidate therapies (170). As shown by the literature, conventional MRI is very sensitive to the pathological changes in patients with MS (171). For example, the number and volume of focal lesions in T_2-weighted MRI is routinely used to evaluate disease burden in MS patients (172). However, due to the lack of specificity of conventional MRI, there is an urgent need to develop alternative tools to improve the measurement of MS pathology, especially de- and re-myelination. Given that structure tensor analysis has shown potential to evaluate myelin integrity in histology images and demonstrated robustness to interpolation and practical feasibility in MR images, I aimed to investigate the utility of structure tensor analysis for assessing the myelin pathology in T_2-weighted images in vivo.

In this chapter, I tested whether structure tensor measures can quantitatively evaluate the in vivo change associated with de- and re-myelination over time in T_2-weighted MRI. Using the same model of de- and re-myelination after lysolecithin deposition, I measured the directional property of focal lesions that were induced in the dorsal column of mouse spinal cords, both at the peak of demyelination and during the period of extensive remyelination in T_2-weighted MR images. Based on our current understanding of remyelination pathology I hypothesize that the repaired lesions will have improved anisotropic properties as compared to the demyelinated lesions but

will be less anisotropic than the healthy white matter, as the remyelinated tissue is not as normal as the healthy tissue (173).

5.2 Methods:

5.2.1 Animal Model And MR Imaging

The lysolecithin model was used to generate demyelination and remyelination as stated in Chapter 3. Eight to13-week old C57B/6 mice were used in this experiment. T_2-weighted MR images of mice spinal cords (C4/5) were obtained at the Experimental Imaging Center at the University of Calgary (figure 5.1). During MR imaging, inhalational isoflurane anesthesia (1.5% in oxygen:N2O 30:70) was delivered by a nose cone. Animals were positioned in a supine position within a 1.9 cm diameter birdcage coil. During the MRI experiments, respiration was monitored and body temperature was kept constant at 37°C by a thermocouple-based system for each mouse. The periods of demyelination (day 7) and remyelination (days 28 to 35) were non-invasively followed by the 9.4 Tesla MRI after lysolecithin deposition (174). MRI protocols included T_2 MRI that were acquired using the following parameters: image sized=256x256, slice thickness= 0.75 mm, repetition time /echo time = 2500ms/15ms and field of view= 2 x 2 cm^2, centered at the lesion center of the spinal cords. As a control for myelin pathology, animals were also imaged at day 0 for normal myelin.

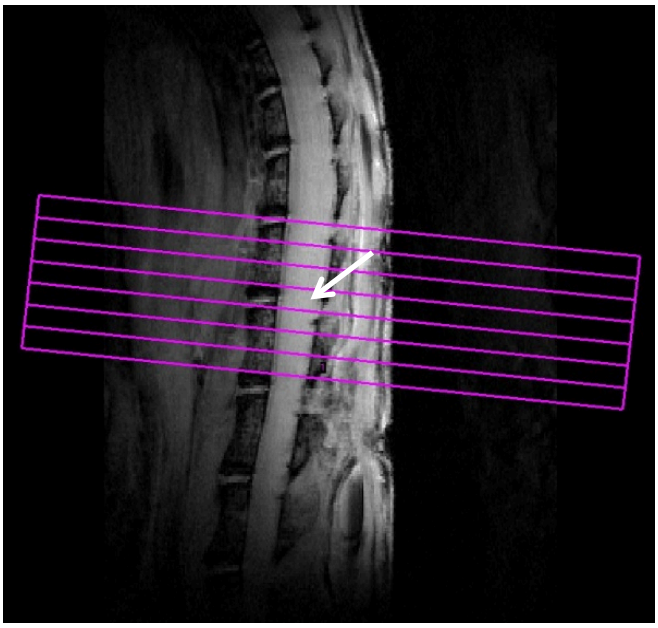

Figure 5.1- *An example of sagittal view set-up of axial T_2-weighted MR image of mouse spinal cord showing the slice positioning for image acquisition. White arrow shows the approximate location of lesions in the spinal cord.*

5.2.2 Image Enhancement

In order to follow the in vivo changes associated with myelin pathology in the lysolecithin model, MR images were obtained at various time points. This may lead to changes in image contrast and homogeneity unrelated to tissue pathology, an inherent issue with MR scanner (175). To ensure standardization of sequential MR images, I normalized their signal intensity across all time points using an enhancement program implemented in ImageJ. This allows for an improved interpretation of the data especially in computer-based analysis (176).

5.2.3 Overview of Enhancement Techniques

Generally, there are two types of enhancement methods: the spatial domain and frequency domain methods (176). The choice of enhancement techniques depends on the task at hand and the final purpose of enhancement. The spatial domain techniques deal with image pixel intensities directly in the image domain. On the other hand, the frequency domain method first converts the image to its spatial frequencies using Fourier transform, which are modified and then transformed back to the image domain using inverse Fourier transform (177). I took advantage of the spatial domain enhancement method known as histogram equalization to standardize MR images in this study. Histogram of an image refers to a graphical representation of pixel intensities and their frequency or count in an image. The information obtained from a histogram has many applications in the field of image compression and segmentation (178). Each pixel value corresponds to a level of pixel brightness where a pixel value of 0 is the darkest pixel and a maximum pixel value of 255 is the brightest pixel in an 8-bit image. Depending on the enhancement method used, the histogram peak (highest frequency of that pixel value) and the distribution of pixel intensities could change (figure 5.2). Although MR images that are obtained at various time points showcase specific and identical anatomical regions, their histograms are not identical. Therefore, histogram enhancement methods are used to standardize these images to enhance accuracy and consistency. Histogram stretching and equalization are two commonly used enhancement methods that are described below. In this chapter, I used the histogram equalization method.

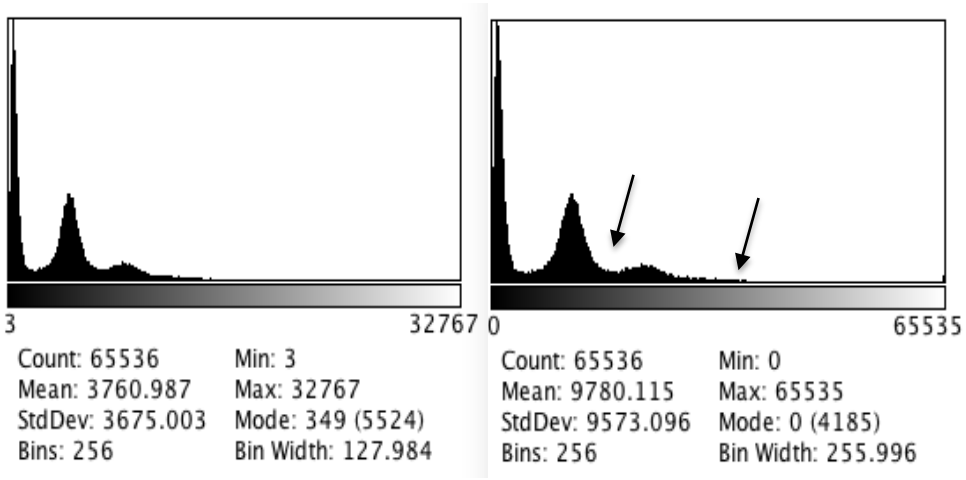

Figure 5.2- *The impact of histogram stretching on the pixel intensity distribution in an image. Panel A shows the histogram of the image prior to enhancement. Panel B shows the image histogram post-enhancement. Arrow shows the "stretching" of histogram to fill more grey levels.*

5.2.4 Histogram Stretching

Mathematically, this is a more basic enhancement method compared to histogram equalization and is commonly used to enhance individual images that were obtained at a single time point. Due to its common use in image processing, histogram stretching is referred to as normalization by the open-access image processing software, ImageJ. After enhancement, the image will have specific minimum and maximum gray levels. This technique standardizes or stretches the image histogram by modifying each pixel value based on the minimum and maximum pixel values in that image (179). Upon normalization, the contrast (distribution of light and dark pixels) of an image increases and additional gray levels are filled. However, the shape of the histogram does not change and the frequency of pixels is not similarly distributed among all gray levels as before. In addition, images with different pre-enhanced histograms continue to have non-similar histograms post enhancement, depending on the inherent minimum and maximum pixel

intensities present in the image. Therefore, the use of this approach for standardization of images that were obtained at various time points is not effective.

5.2.5 Histogram Equalization

Histogram equalization refers to the spreading of pixel intensities that present in high count in an image along the total range of values, where the shape and distribution of the histogram of the output image is different from that of the input image (178). The histogram of images that were obtained at various time points appear very similar or "equal", as the name suggests, to each other after standardization, making this approach a more suitable technique for normalization of time-series data. This method uses a more advanced set of statistical steps to achieve a better enhanced image with a less global effect on pixel values, as high frequency pixels are preserved better in the output image (180). Computationally, this approach uses probability mass function and cumulative distributive function as its first and second steps towards normalization (181). Probability mass function gives the probability of each gray level in a given data set. Cumulative distributive function is basically the step-wise sum of all probabilities that are calculated in the previous step. To find the new, normalized gray level, the cumulative distributive function is multiplied by its corresponding gray level value minus one (originally, each cumulative distributive function value has a corresponding gray level). This normalized grey level value is then mapped into the frequency of pixels, generating a new histogram. Compared to histogram stretching, this technique uses a more global approach in data normalization. It uses simple probability to normalized histograms, creating more uniform histograms, while preserving high frequency pixels regardless of varying maximum and minimum pixel values in individual images.

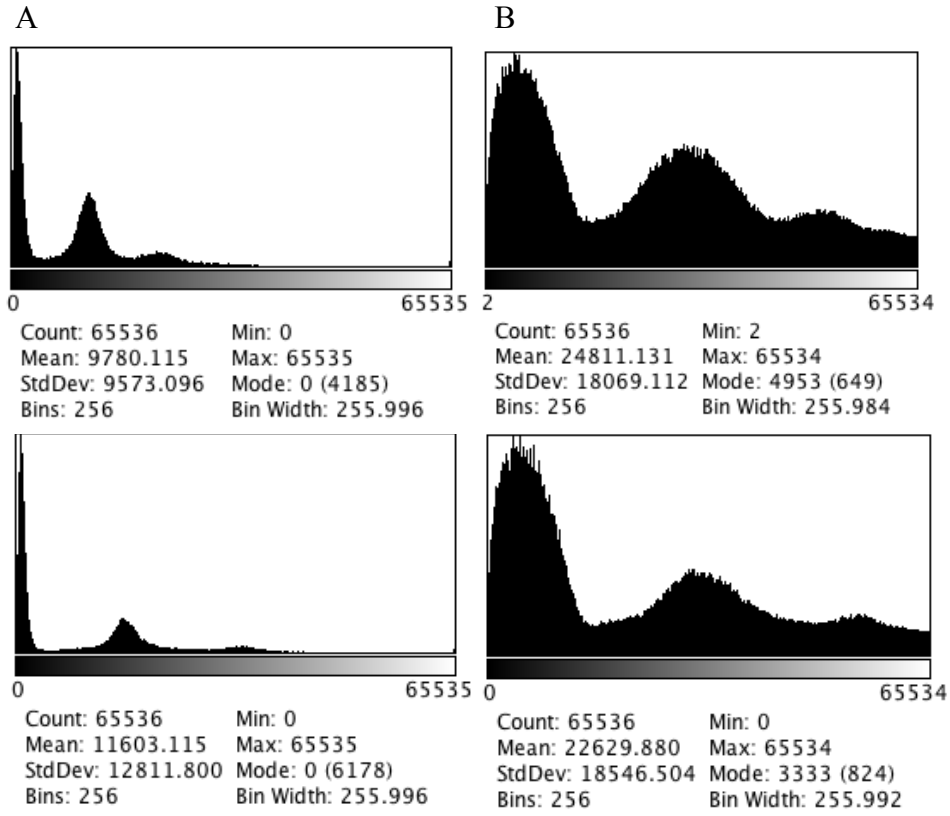

Figure 5.3- *Impact of histogram stretching on pixel intensity distribution compare to histogram equalization. Panel A shows the histogram of 2 different MR images after histogram stretching. Panel B shows the histogram of the same two images after histogram equalization. Histograms of images enhanced by the equalization method are more similar than the images enhanced by the stretching method.*

5.2.6 Structure Tensor Analysis

Following histogram equalization, MR images of the demyelinated and remyelinated lesions were evaluated using structure tensor analysis approach as described in chapter 3. Outcome measures were obtained based on the interpolated 512x512 images with the use of 11x11-pixel ROIs. To ensure assessing the same tissue over time, the ROIs were positioned at the same location in the dorsal column within each mouse. The b-spline interpolation method verified in

chapter 4 was used to interpolate the original 256x 256 images to 512x512. Structure tensor analysis was performed in MR images obtained at day 0 with healthy myelin, day 7 with severe demyelination, and days 28-35 with mostly remyelination. Images from the remyelination period were combined and shown as one time-point. (182).

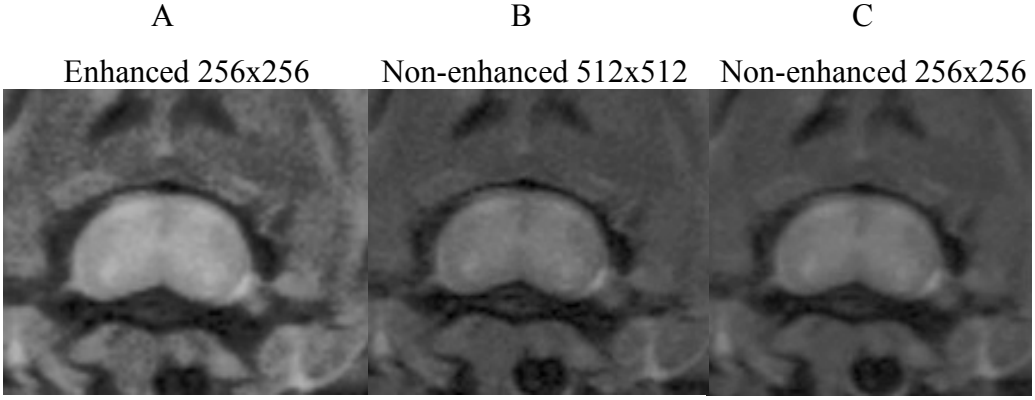

Figure 5.4- *ROIs from axial enhanced and non-enhanced T_2-weighted images of mice cervical spinal cord. Panel A shows the same anatomical area in a histogram-equalized enhanced 256x256 image. Panel B shows the same anatomical area in non-enhanced, b-spline-interpolated 512x512 image. Panel C is an ROI from a non-enhanced 256x256 images.*

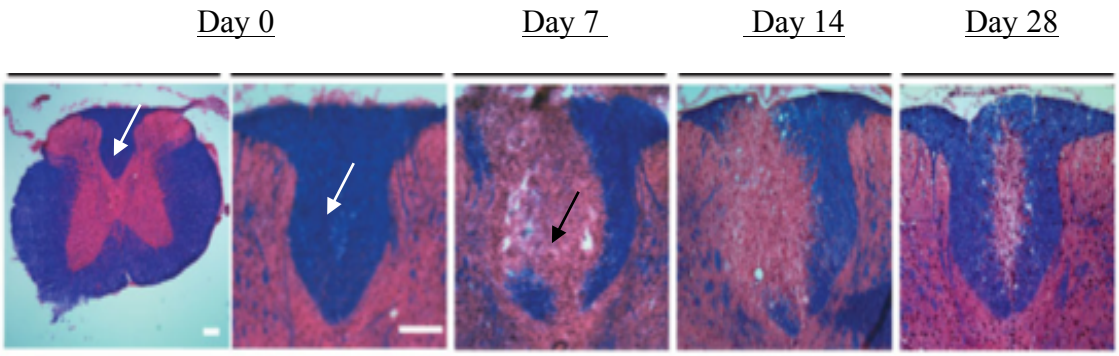

Figure 5.5- *Representative histology images of demyelination and remyelination in the dorsal column of lysolecithin mouse model. Healthy, myelinated dorsal column is shown by the white arrows. Both zoomed in and out images of the healthy dorsal column are shown at Day 0 for comparative observations. Demyelination of the dorsal column 7-14 days post injection is shown by the black arrows. Spontaneous remyeliation is evident at day 28 and beyond (in C57B/6). The figure is obtained and modified Lau et al, Ann Neurol, 2012 (13).*

5.3 Statistics

All analyses were conduced using Graphpad Prism version 5.0. D'Agostino & Pearson omnibus normality test was conducted to test sample normality. Based on a normality test, the generated values from these ROIs were not normally distributed. Therefore, I used non-parametric one-way ANOVA (Kruskal- Wallis) to evaluate the differences between coherency and entropy of myelinated, demyelinated and remyelinated tissues. Dunn's post hoc test was used to compare pair-wise differences between myelinated, demyelinated, and remyelinated groups. The $p<0.05$ was considered significant in all cases.

5.4 Results

A total of 90 MR images were obtained from all 3 time-points for analysis. After quality control, 47 were eventually assessed quantitatively. MR images with poor resolution or those that were affected by motion artefacts were excluded.

5.4.1 Fully Myelinated And Remyelinated Tissues Had A Significantly Higher Energy Than Demyelinated Tissue

Non-parametric one-way ANOVA assessment of energy for the fully myelinated, demyelinated, and remyelinated tissues showed significant difference between groups ($P<0.0001$). Dunn's post hoc test indicated a significantly higher energy for the remyelinated lesions (mean ± standard error = $2.16x\ 10^6 \pm 184072$) compared to the demyelinated lesions ($P<0.0001$). No significant difference was found between the healthy, myelinated tissue ($1.632x10^6 \pm 194648$) and the other two groups. The demyelinated lesions had the smallest mean energy ($1.025x10^6 \pm 189086$).

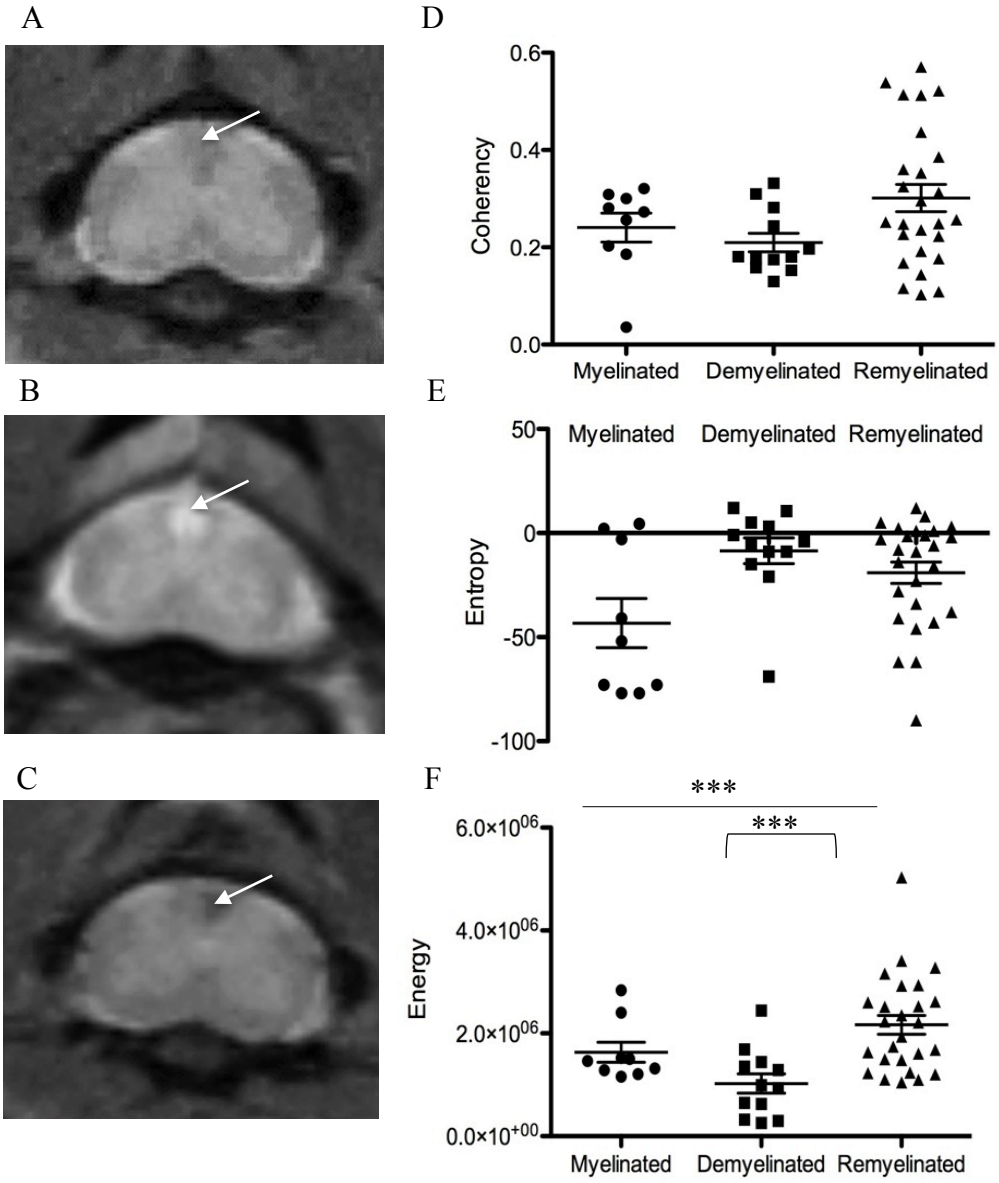

Figure 5.6- *Example of T_2-weighted MR images of mice spinal cords of the lysolecithin mouse and scatter plots of tissue directional properties from the whole study. Panel A-C correspond to images of the fully myelinated, demyelinated and remyelinated dorsal column. Panel D-F show the scatter plots of coherency, energy and entropy of these tissues. Arrows point out the affected*

*dorsal column. Dunn's test indicated differences between the energy of de- and re-myelinated tissu**es** ($p<0.0001$). Bars represent 95% confidence interval and standard errors.*

5.4.2 Tissues With Higher Myelin Integrity Showed a Trend for Better Coherency And Lower Angular Entropy

While not significant ($p>0.05$), the myelinated (0.2406 ± 0.029) and remyelinated (0.3012 ± 0.027) groups had better coherency than the demyelinated group (mean ± standard error = 0.2098 ± 0.019). The same trend was observed for the entropy measure ($p>0.05$). The myelinated healthy tissue had the lowest angular entropy (-43.29 ± 11.83) followed by the remyelinated lesions (-19.05 ± 5.08), and the demyelinated lesions had the highest entropy (-8.542 ± 6.18). Based on the one-way ANOVA and Dunn's post hoc analyses, there were no significant differences between demyelinated, remyelinated, and myelinated groups in either coherency or entropy ($p>0.05$).

5.5 Discussion and Summary

In this study, standard MR images of fully myelinated, completely demyelinated, and mostly remyelinated dorsal column of the lysolecithin mice were used to validate the potential of structure tensor analysis as a measure of tissue integrity and anisotropy. Although significant differences were only found for the energy analyses, this in vivo study showed consistent trend for better coherency and lower angular entropy for myelinated and remyelinated tissues compared to the demyelinated tissue. This is in line with the prediction that fully myelinated and

remyelinated tissues have a higher anisotropy and better organization than the injured, demyelinated tissue.

Based on this pilot study, I found significantly higher energy in the remyelinated lesions than in the demyelinated lesions. In fact, the energy of remyelinated lesions was approximately twice as large as the energy of demyelinated lesions. This is consistent with histological evidence that areas of greater myelin integrity have a better directional organization (183). Likewise, the energy of myelinated white matter was 59 percent higher than the energy of demyelinated lesions. Although the difference between these two tissues was not significant, this again illustrates a higher degree of directional organization for tissues with higher myelin content. Based on these results, the repair of myelin sheaths attempts to restore the diminished directionality caused by demyelination. Mathematically, this improvement in myelin pathology reflects an increased sum of eigenvalues corresponding to the two dominant eigenvectors in the image. A larger sum of eigenvalues corresponds to better tissue organization, which is attributed to myelin repair based on this model.

Findings from analyses of coherency and angular entropy for the myelinated and remyelinated groups suggest increased anisotropy and regularity in the microstructure of these tissues compared to the demyelinated tissue. Despite statistically non-significant results, the coherency of the myelinated and remyelinated tissues was respectively 15 and 44 percent better than that of the demyelinated. Moreover, the results of the angular entropy analyses of all three tissue types showed a lower degree of directional heterogeneity for the more uniformed, myelinated regions compared to the damaged, demyelinated lesions. This was evident as the remyelinated tissue was

60 percent more homogenous than the demyelinated tissue. The same trend was noted for the fully myelinated tissue where the degree of angular homogeneity was 4 times better than the demyelinated lesions. Although the results showed a difference in directional property between demyelinated and remyelinated tissues and the trends were consistent among all groups, this was a small pilot study that evaluated a total of 47 ROIs. This goal was to test the feasibility of using structure tensor analysis in standard MR images in vivo. Further work with sufficiently large sample size that warrants a normal distribution is needed.

Currently, there is strong interest in medical imaging research to develop quantitative measures of structure directionality to enhance the evaluation of tissue pathology. However, few existing techniques are specific to de- or re-myelination. For instance, quantitative acquisition techniques such as DTI, provides us with valuable information about the alignment and anisotropy of white matter tracts based on the microstructural integrity of the tissue. Specifically, tissue integrity is estimated based on the Brownian motion of water molecules, preferably along the long axis of nerve fibers that has fewer barriers than the radial direction packed with myelin bilayers. Changes in DTI measurements can be due to alterations in myelin-associated tissue integrity, but are not dedicated to de- or re-myelination (142).

Based on post-processing of standard MR images, several quantitative techniques have demonstrated potential to evaluate subtle changes in tissue pathology, including MRI texture analysis. Texture analysis of the white matter in MS patients has previously distinguished the active states of various lesions with considerable accuracy (184). A recent texture study evaluated the differences between active lesions and compared them to the texture properties of

NAWM and chronic lesions. Although a small sample size, this study found significant differences between tissue groups (185), a task unlikely to be achieved by the human eye. Similar to the image post-processing nature of texture analysis on standard MR images, structure tensor analysis may be an alternative approach for assessing tissue coherency and organization. Instead of assessing the texture of image pixels, structure tensor analysis of an image calculates a set of directional metrics that is based on tissue alignment (127). Based on the calculation of tissue directional properties, this work showed the potential to distinguish between directional organizations of different tissues with different myelin activity. According to T_2-weighted MR images, energy appeared to be the most specific measure compared to other measures in this particular sample. The result of energy analysis was also consistent with my previous findings of histology in chapter 3; however, in that study, I also identified coherency to be the outcome with a relatively higher specificity to myelin activity. This discrepancy could be due to the size of samples and the resolution of images studied. The coherency measure showed a better specificity in the analysis of high-resolution histology images whereas energy was deemed to be superior in the assessment of MR images that had a resolution of ~10 times smaller. A serial large-sample study is required to confirm these findings in the future.

In summary, structure tensor analysis of de- and re-myelinated dorsal column of lysolecithin mice has shown potential to evaluate myelin-related directionality based on clinically feasible MR images. This is particularly evident for measures of energy based on this small sample. The post-hoc analysis following ANOVA showed a significantly higher energy for the remyelinated tissue than demyelinated tissue, although no significant differences were noted between other groups. Overall, there was a consistent trend for higher energy, coherency, and lower entropy in

fully myelinated and remyelinated tissues compared to the demyelinated tissue. This is consistent with the hypothesis that demyelination and remyelination change the directional property of white matter and that these changes can be quantitatively detected by structure tensor analysis.

Chapter Six: **Conclusion and Future Directions**

6.1 Summary of Research Findings

The overall goal of this thesis project was to test the hypothesis that structure tensor-based outcome measures can be utilized to identify changes in tissue directionality and anisotropy caused by demyelination and remyelination. In this regard, I used structure tensor analysis to study the myelin-related directionality in the white matter of spinal cords from the lysolecithin mice, a model of demyelination followed by spontaneous remyelination. I tested this method using both histological and MR images and found encouraging results showing that there was better alignment and organization but lower directional disorder in tissues with higher myelin content than tissues with loss of myelin. For technical validation, I also confirmed the robustness of structure tensor analysis to different image interpolation techniques and to changes in image size. Collectively, my results support the use of structure tensor analysis to assess myelin integrity based on standard MR images and warrants further validation.

Histology is the standard tool for evaluation of anatomy and tissue microstructure ex vivo. Using stained histology images of fully myelinated (healthy), completely demyelinated (lesion) and partially demyelinated (lesion border) tissues, I found significant differences between tissues with different myelin integrity, and that tissues with higher myelin content had better coherency, higher energy, and lower entropy. These findings are consistent with our current understanding of injured neuronal structure where tissue anisotropy and uniformity are diminished in demyelinated lesions (186). Moreover, the study of epicentre and distant areas of a lesion and lesion border illustrated no directional differences between injury sites in the same type of tissue, indicating that the severity of the tissue damage such as demyelination would be an important

consideration of tissue directionality. Consequently, the evaluation of histological images in this part of the thesis served as a foundation for future testing of the ability of structure tensor analysis.

In order to study the in vivo pathology of de- and re-myelination, conventional MR images were utilized as they are routinely applied in the standard care of patients. Prior to the use of structure tensor analysis to measure pathology in T_2-weighted MR images, I studied the robustness of structure tensor-based outcome measures to different interpolation methods, an image-processing technique commonly used in various image manipulation steps. I also evaluated the impact of interpolation on eigenvectors and eigenvalues, characteristic features that reflect the principal magnitude and directions of the oriented structures in an image. Interpolation is a critical step in image co-registration that is used to align different image for precise comparison; down- or up-sampling of data sets is often involved. Through comprehensive testing, I found that the coherency measure is the most robust to image interpolation and the b-spline approach to be the most reliable interpolation method. Further analyses of eigenvectors and eigenvalues of interpolated MR images suggested the robustness of these characteristics to b-spline interpolation. Therefore, I used the b-spline interpolation method in the next aim to investigate the potential of structure tensor analysis in standard MR images, as detailed below.

As a preliminary in vivo study, I used structure tensor analysis to identify de- and re-myelination in T_2-weighted MR images acquired from the lysolecithin animal model. I evaluated the directional property of fully myelinated, completely demyelinated, and remyelinated tissues in the dorsal column of mouse spinal cords. I found that there were significant differences in the

energy measure through a non-parametric one-way ANOVA. In particular, the post hoc analysis showed a significantly better energy indicating improved fiber organization for remyelinated lesions than for demyelinated lesions. I also discovered that there was a consistent trend of higher coherency and lower entropy for tissues with higher myelin content, in line with my previous observations in histology images and the expectation that myelinated tissue is more uniform and homogeneous leading to better directional organization than demyelinated tissues.

6.2 Significance of Research

Potentially, structure tensor based-measures may be used as simple, quantitative measures of tissue coherency and anisotropy for the evaluation of de- and re-myelination in standard MR images in the future. As clinical trials for developing new MS therapeutics continue, there will be a growing need for quantitative measures that demonstrate practical feasibility and imaging efficiency to evaluate myelin integrity. Based on post-processing of conventional MR images, structure tensor analysis may have the potential to become an option for assessing the myelin property in demyelinated MS lesions that recover over time. This should help advance the diagnosis and management of the disease, and may eventually promote the discovery of repair medicines for patients with MS and other demyelinating diseases, with further validation.

6.3 Limitations

This work was based on the use of the lysolecithin mouse model. While it provides an excellent opportunity to study de- and re-myelination, I did not have the chance to evaluate the impact of other pathological components commonly seen in MS such as inflammation, edema, axonal damage, and astrocyte scarring on tissue directionality. In addition, for technical validation of

structure tensor analysis, I only focused on the testing of three commonly used interpolation techniques. A comprehensive study of other techniques available in the literature would be valuable to improve the understanding of the new image analysis method. Moreover, for the in vivo analysis of de- and re-myelinated lesions, the sample size was small and histological images were not available for this specific study for direct comparison with MR images. Nonetheless, this lysolecithin model has been thoroughly studied in the literature and its time-series histology is very well understood by others and our collaborators (182). Finally, the current implementation of structure tensor analysis is limited to 2D images. However, based on a recent study, strong correlations were found between structure tensor-based 2D indices and 3D DTI outcomes (130). Further validation is warranted.

6.4 Future Directions

In the future, structure tensor analysis can be investigated in several directions. In a similar manner, structure tensor analysis can be tested for its ability to evaluate the directionality of nerve fibers following axonal injury in the white matter, using either histological or MR images. This will verify to which extent the changes reported here are true reflections of myelin regularity, in comparison with axonal health. Further research could also study the relationship between outcomes of structure tensor analysis and DTI to evaluate demyelination and remyelination, as previous research has suggested that structure tensor analysis is a useful tool to validate DTI metrics (130). Furthermore, using existing or newly acquired MR images of MS patients at various time points could test the potential of structure tensor analysis in detecting changes of myelin-related directionality in different types of MS lesions, including shadow plaques, as compared to NAWM and intact whiter matter. Overall, I am very excited about the

potential and future applications of structure tensor analysis as a new measure of tissue regularity and anisotropy and believe that it may become a promising new tool in the imaging of MS pathology, particularly regarding de- and re-myelination.

References

1. Marrie R, Yu N, Blanchard J, Leung S, Elliott L. The rising prevalence and changing age distribution of multiple sclerosis in Manitoba. Neurology. 2010;74(6):465-71.

2. Hauser SL, Oksenberg JR. The neurobiology of multiple sclerosis: genes, inflammation, and neurodegeneration. Neuron. 2006;52(1):61-76.

3. Myhr K-M, Riise T, Vedeler C, Nortvedt M, Grønning M, Midgard R, et al. Disability and prognosis in multiple sclerosis: demographic and clinical variables important for the ability to walk and awarding of disability pension. Multiple sclerosis. 2001;7(1):59-65.

4. Lassmann H, Brück W, Lucchinetti C. Heterogeneity of multiple sclerosis pathogenesis: implications for diagnosis and therapy. Trends in molecular medicine. 2001;7(3):115-21.

5. Chari DM. Remyelination in multiple sclerosis. International review of neurobiology. 2007;79:589-620.

6. Poloni G, Minagar A, Haacke EM, Zivadinov R. Recent developments in imaging of multiple sclerosis. The neurologist. 2011;17(4):185-204.

7. Beaulieu C. The basis of anisotropic water diffusion in the nervous system–a technical review. NMR in biomedicine. 2002;15(7-8):435-55.

8. Klingberg T, Vaidya CJ, Gabrieli JD, Moseley ME, Hedehus M. Myelination and organization of the frontal white matter in children: a diffusion tensor MRI study. Neuroreport. 1999;10(13):2817-21.

9. Smith K, Blakemore W, McDonald W. Central remyelination restores secure conduction. 1979.

10. He B, Wu JP, Chen HH, Kirk TB, Xu J. Elastin fibers display a versatile microfibril network in articular cartilage depending on the mechanical microenvironments. Journal of

orthopaedic research : official publication of the Orthopaedic Research Society. 2013 Sep;31(9):1345-53.

11. Rezakhaniha R, Agianniotis A, Schrauwen JT, Griffa A, Sage D, Bouten CV, et al. Experimental investigation of collagen waviness and orientation in the arterial adventitia using confocal laser scanning microscopy. Biomechanics and modeling in mechanobiology. 2012 Mar;11(3-4):461-73..

12. Budde MD, Annese J. Quantification of anisotropy and fiber orientation in human brain histological sections. Frontiers in integrative neuroscience. 2013;7:3.

13. Lau LW, Keough MB, Haylock-Jacobs S, Cua R, Doring A, Sloka S, et al. Chondroitin sulfate proteoglycans in demyelinated lesions impair remyelination. Annals of neurology. 2012 Sep;72(3):419-32.

14. Yu O, Steibel J, Mauss Y, Guignard B, Eclancher B, Chambron J, et al. Remyelination assessment by MRI texture analysis in a cuprizone mouse model. Magnetic resonance imaging. 2004;22(8):1139-44.

15. Rosati G. The prevalence of multiple sclerosis in the world: an update. Neurological sciences. 2001;22(2):117-39.

16. Love S. Demyelinating diseases. Journal of clinical pathology. 2006 Nov;59(11):1151-9. PubMed PMID: 17071802.

17. Luchetti S, van Eden CG, Schuurman K, van Strien ME, Swaab DF, Huitinga I. Gender Differences in Multiple Sclerosis: Induction of Estrogen Signaling in Male and Progesterone Signaling in Female Lesions. Journal of Neuropathology & Experimental Neurology. 2014;73(2):123-35.

18. Thompson A, Polman C, Miller D, McDonald W, Brochet B, Montalban XFM, et al. Primary progressive multiple sclerosis. Brain : a journal of neurology. 1997;120(6):1085-96.

19. Compston A, Coles A. Multiple sclerosis. Lancet. 2008 Oct 25;372(9648):1502-17.

20. Shivane AG, Chakrabarty A. Multiple sclerosis and demyelination. Current Diagnostic Pathology. 2007;13(3):193-202.

21. Matute C, Ransom BR. Roles of white matter in central nervous system pathophysiologies. ASN neuro. 2012;4(2).

22. Franklin RJ, Ffrench-Constant C. Remyelination in the CNS: from biology to therapy. Nature reviews Neuroscience. 2008 Nov;9(11):839-55.

23. Franklin RJ, ffrench-Constant C, Edgar JM, Smith KJ. Neuroprotection and repair in multiple sclerosis. Nature reviews Neurology. 2012 Nov 5;8(11):624-34.

24. Bø L, Esiri M, Evangelou N, Kuhlmann T. Demyelination and remyelination in multiple sclerosis. Myelin Repair and Neuroprotection in Multiple Sclerosis: Springer; 2013. p. 23-45.

25. Prineas J, Connell F. Remyelination in multiple sclerosis. Annals of neurology. 1979;5(1):22-31.

26. Deloire-Grassin M, Brochet B, Quesson B, Delalande C, Dousset V, Canioni P, et al. In vivo evaluation of remyelination in rat brain by magnetization transfer imaging. Journal of the neurological sciences. 2000;178(1):10-6.

27. Kotter MR, Setzu A, Sim FJ, Van Rooijen N, Franklin RJ. Macrophage depletion impairs oligodendrocyte remyelination following lysolecithin-induced demyelination. Glia. 2001;35(3):204-12.

28. Kotter MR, Zhao C, van Rooijen N, Franklin RJ. Macrophage-depletion induced impairment of experimental CNS remyelination is associated with a reduced oligodendrocyte

progenitor cell response and altered growth factor expression. Neurobiology of disease. 2005;18(1):166-75.

29. Patrikios P, Stadelmann C, Kutzelnigg A, Rauschka H, Schmidbauer M, Laursen H, et al. Remyelination is extensive in a subset of multiple sclerosis patients. Brain : a journal of neurology. 2006;129(12):3165-72.

30. Arnett HA, Mason J, Marino M, Suzuki K, Matsushima GK, Ting JP-Y. TNFα promotes proliferation of oligodendrocyte progenitors and remyelination. Nature neuroscience. 2001;4(11):1116-22.

31. Gaudet AD, Popovich PG, Ramer MS. Wallerian degeneration: gaining perspective on inflammatory events after peripheral nerve injury. J Neuroinflammation. 2011;8(1):110.

32. Makoukji J, Belle M, Meffre D, Stassart R, Grenier J, Shackleford G, et al. Lithium enhances remyelination of peripheral nerves. Proceedings of the National Academy of Sciences of the United States of America. 2012 Mar 6;109(10):3973-8.

33. Jacobson BE. Tracking and Manipulating Myelin Dynamics after Spinal Cord Injury: University of Washington; 2011.

34. Miller DJ, Asakura K, Rodriguez M. Central nervous system remyelination clinical application of basic neuroscience principles. Brain pathology. 1996;6(3):331-44.

35. Schauf C, Davis FA. Impulse conduction in multiple sclerosis: a theoretical basis for modification by temperature and pharmacological agents. Journal of Neurology, Neurosurgery & Psychiatry. 1974;37(2):152-61.

36. Trapp BD, Ransohoff R, Rudick R. Axonal pathology in multiple sclerosis: relationship to neurologic disability. Current opinion in neurology. 1999;12(3):295-302.

37. Lucchinetti CF, Brück W, Rodriguez M, Lassmann H. Distinct patterns of multiple sclerosis pathology indicates heterogeneity in pathogenesis. Brain pathology. 1996;6(3):259-74.

38. Pavelko KD, Van Engelen BG, Rodriguez M. Acceleration in the rate of CNS remyelination in lysolecithin-induced demyelination. The Journal of neuroscience. 1998;18(7):2498-505.

39. HALL SM. The effect of injections of lysophosphatidyl choline into white matter of the adult mouse spinal cord. Journal of Cell Science. 1972;10(2):535-46.

40. Smith K, Blakemore W, McDonald W. The restoration of conduction by central remyelination. Brain: a journal of neurology. 1981;104(2):383-404.

41. Felts PA, Smith KJ. Conduction properties of central nerve fibers remyelinated by Schwann cells. Brain research. 1992;574(1):178-92.

42. Jeffery N, Blakemore W. Remyelination of mouse spinal cord axons demyelinated by local injection of lysolecithin. Journal of neurocytology. 1995;24(10):775-81.

43. Irvine K, Blakemore W. Remyelination protects axons from demyelination-associated axon degeneration. Brain : a journal of neurology. 2008;131(6):1464-77.

44. Ransohoff RM. Animal models of multiple sclerosis: the good, the bad and the bottom line. Nature neuroscience. 2012 Aug;15(8):1074-7.

45. Torkildsen Ø, Brunborg L, Myhr KM, Bø L. The cuprizone model for demyelination. Acta Neurologica Scandinavica. 2008;117(s188):72-6.

46. Matsushima GK, Morell P. The neurotoxicant, cuprizone, as a model to study demyelination and remyelination in the central nervous system. Brain Pathology. 2001;11(1):107-16.

47. Venturini G. Enzymic activities and sodium, potassium and copper concentrations in mouse brain and liver after cuprizone treatment in vivo. Journal of neurochemistry. 1973;21(5):1147-51.

48. Suzuki K, Kikkawa Y. Status spongiosus of CNS and hepatic changes induced by cuprizone (biscyclohexanone oxalyldihydrazone). The American journal of pathology. 1969;54(2):307.

49. Xiao L, Xu H, Zhang Y, Wei Z, He J, Jiang W, et al. Quetiapine facilitates oligodendrocyte development and prevents mice from myelin breakdown and behavioral changes. Molecular psychiatry. 2007;13(7):697-708.

50. Irvine K, Blakemore W. Age increases axon loss associated with primary demyelination in cuprizone-induced demyelination in C57BL/6 mice. Journal of neuroimmunology. 2006;175(1):69-76.

51. McMahon EJ, Suzuki K, Matsushima GK. Peripheral macrophage recruitment in cuprizone-induced CNS demyelination despite an intact blood–brain barrier. Journal of neuroimmunology. 2002;130(1):32-45.

52. Blakemore W. Observations on oligodendrocyte degeneration, the resolution of status spongiosus and remyelination in cuprizone intoxication in mice. Journal of neurocytology. 1972;1(4):413-26.

53. Trip SA, Miller DH. Imaging in multiple sclerosis. Journal of neurology, neurosurgery, and psychiatry. 2005 Sep;76 Suppl 3:iii11-iii8.

54. Nusbaum AO, Lu D, Tang CY, Atlas SW. Quantitative diffusion measurements in focal multiple sclerosis lesions: correlations with appearance on TI-weighted MR images. AJR American journal of roentgenology. 2000 Sep;175(3):821-5.

55. Brex P, Parker G, Leary S, Molyneux P, Barker G, Davie C, et al. Lesion heterogeneity in multiple sclerosis: a study of the relations between appearances on T1 weighted images, T1 relaxation times, and metabolite concentrations. Journal of Neurology, Neurosurgery & Psychiatry. 2000;68(5):627-32.

56. Sahraian M, Radue EW, Haller S, Kappos L. Black holes in multiple sclerosis: definition, evolution, and clinical correlations. Acta Neurologica Scandinavica. 2010;122(1):1-8.

57. Van Walderveen MA, Barkhof F, Pouwels PJ, Van Schijndel RA, Polman CH, Castelijns JA. Neuronal damage in T1-hypointense multiple sclerosis lesions demonstrated in vivo using proton magnetic resonance spectroscopy. Annals of neurology. 1999;46(1):79-87.

58. Hodgson RJ. (v) The basic science of MRI. Orthopaedics and Trauma. 2011;25(2):119-30.

59. Leary S, Giovannoni G, Howard R, Miller D, Thompson A. Multiple sclerosis and demyelinating diseases. Neurology: A Queen Square Textbook. 2009:411-47.

60. Sahraian MA, Radue E-W. MS Lesions in T2-Weighted Images. MRI Atlas of MS Lesions: Springer; 2008. p. 3-34.

61. Zhang Y. MRI texture analysis in multiple sclerosis. Journal of Biomedical Imaging. 2012;2012:2.

62. Li DK, Paty DW. Magnetic resonance imaging results of the PRISMS trial: A randomized, double-blind, placebo-controlled study of interferon-β1a in relapsing-remitting multiple sclerosis. Annals of neurology. 1999;46(2):197-206.

63. Gadian D, Payne J, Bryant D, Young I, Carr D, Bydder G. Gadolinium-DTPA as a contrast agent in MR imaging-theoretical projections and practical observations. Journal of computer assisted tomography. 1985;9(2):242-51.

64. Miller D, Rudge P, Johnson G, Kendall B, Macmanus D, Moseley I, et al. Serial gadolinium enhanced magnetic resonance imaging in multiple sclerosis. Brain : a journal of neurology. 1988;111(4):927-39.

65. Nathoo N, Yong VW, Dunn JF. Using magnetic resonance imaging in animal models to guide drug development in multiple sclerosis. Multiple Sclerosis Journal. 2014;20(1):3-11.

66. Barkhof F. The clinico-radiological paradox in multiple sclerosis revisited. Current opinion in neurology. 2002 Jun;15(3):239-45.

67. Brück W, Bitsch A, Kolenda H, Brück Y, Stiefel M, Lassmann H. Inflammatory central nervous system demyelination: correlation of magnetic resonance imaging findings with lesion pathology. Annals of neurology. 1997;42(5):783-93.

68. Barkhof F, Brück W, De Groot CJ, Bergers E, Hulshof S, Geurts J, et al. Remyelinated lesions in multiple sclerosis: magnetic resonance image appearance. Archives of neurology. 2003;60(8):1073-81.

69. Verhey LH, Sled JG. Advanced Magnetic Resonance Imaging in Pediatric Multiple Sclerosis. Neuroimaging Clinics of North America. 2013;23(2):337-54.

70. Kapeller P, McLean MA, Griffin CM, Chard D, Parker GJ, Barker GJ, et al. Preliminary evidence for neuronal damage in cortical grey matter and normal appearing white matter in short duration relapsing-remitting multiple sclerosis: a quantitative MR spectroscopic imaging study. Journal of neurology. 2001 Feb;248(2):131-8.

71. Dousset V, Grossman R, Ramer K, Schnall M, Young L, Gonzalez-Scarano F, et al. Experimental allergic encephalomyelitis and multiple sclerosis: lesion characterization with magnetization transfer imaging. Radiology. 1992;182(2):483-91.

72. Cercignani M, Bozzali M, Iannucci G, Comi G, Filippi M. Magnetisation transfer ratio and mean diffusivity of normal appearing white and grey matter from patients with multiple sclerosis. Journal of Neurology, Neurosurgery & Psychiatry. 2001;70(3):311-7.

73. Rocca MA, Mastronardo G, Rodegher M, Comi G, Filippi M. Long-term changes of magnetization transfer–derived measures from patients with relapsing-remitting and secondary progressive multiple sclerosis. American journal of neuroradiology. 1999;20(5):821-7.

74. Filippi M, Rocca MA. Magnetization transfer magnetic resonance imaging of the brain, spinal cord, and optic nerve. Neurotherapeutics. 2007;4(3):401-13.

75. Santos AC, Narayanan S, de Stefano N, Tartaglia MC, Francis SJ, Arnaoutelis R, et al. Magnetization transfer can predict clinical evolution in patients with multiple sclerosis. Journal of neurology. 2002 Jun;249(6):662-8.

76. Chen JT, Collins DL, Atkins HL, Freedman MS, Arnold DL. Magnetization transfer ratio evolution with demyelination and remyelination in multiple sclerosis lesions. Annals of neurology. 2008;63(2):254-62.

77. Chen JT, Easley K, Schneider C, Nakamura K, Kidd GJ, Chang A, et al. Clinically feasible MTR is sensitive to cortical demyelination in MS. Neurology. 2013 Jan 15;80(3):246-52.

78. Kelemen A, Liang Y. Multi-Center Correction Functions for Magnetization Transfer Ratios of MRI Scans. J Health Med Informat S. 2011;3:2.

79. Vavasour IM, Laule C, Li DK, Traboulsee AL, MacKay AL. Is the magnetization transfer ratio a marker for myelin in multiple sclerosis? Journal of Magnetic Resonance Imaging. 2011;33(3):710-8.

80. Schmierer K, Scaravilli F, Altmann DR, Barker GJ, Miller DH. Magnetization transfer ratio and myelin in postmortem multiple sclerosis brain. Annals of neurology. 2004;56(3):407-15.

81. Arnold DL, Dalton CM, Schmierer K, Pike GB, Miller DH. Imaging of Demyelination and Remyelination in Multiple Sclerosis. Myelin Repair and Neuroprotection in Multiple Sclerosis: Springer; 2013. p. 233-53.

82. Mackay A, Whittall K, Adler J, Li D, Paty D, Graeb D. In vivo visualization of myelin water in brain by magnetic resonance. Magnetic Resonance in Medicine. 1994;31(6):673-7.

83. Laule C, Leung E, Li DK, Traboulsee A, Paty D, MacKay A, et al. Myelin water imaging in multiple sclerosis: quantitative correlations with histopathology. Multiple Sclerosis. 2006;12(6):747-53.

84. Laule C, Vavasour I, Moore G, Oger J, Li D, Paty D, et al. Water content and myelin water fraction in multiple sclerosis. Journal of neurology. 2004;251(3):284-93.

85. Vavasour I, Laule C, Li D, Oger J, Moore G, Traboulsee A, et al. Longitudinal changes in myelin water fraction in two MS patients with active disease. Journal of the neurological sciences. 2009;276(1):49-53.

86. Gareau PJ, Rutt BK, Karlik SJ, Mitchell JR. Magnetization transfer and multicomponent T2 relaxation measurements with histopathologic correlation in an experimental model of MS. Journal of Magnetic Resonance Imaging. 2000;11(6):586-95.

87. Webb S, Munro CA, Midha R, Stanisz GJ. Is multicomponent T2 a good measure of myelin content in peripheral nerve? Magnetic resonance in medicine. 2003;49(4):638-45.

88. Levesque IR. Quantitative magnetic resonance imaging of magnetization transfer and T2 relaxation in human white matter pathology: McGill University; 2009.

89. Alonso-Ortiz E, Levesque IR, Pike GB. MRI-based myelin water imaging: A technical review. Magnetic resonance in medicine : official journal of the Society of Magnetic Resonance in Medicine / Society of Magnetic Resonance in Medicine. 2014 Mar 6.

90. Guo J, Ji Q, Reddick WE. Multi-slice myelin water imaging for practical clinical applications at 3.0 T. Magnetic Resonance in Medicine. 2013;70(3):813-22.

91. Du YP, Chu R, Hwang D, Brown MS, Kleinschmidt-DeMasters BK, Singel D, et al. Fast multislice mapping of the myelin water fraction using multicompartment analysis of T 2* decay at 3T: a preliminary postmortem study. Magnetic Resonance in Medicine. 2007;58(5):865-70.

92. Pfefferbaum A, Sullivan EV, Hedehus M, Lim KO, Adalsteinsson E, Moseley M. Age-related decline in brain white matter anisotropy measured with spatially corrected echo-planar diffusion tensor imaging. Magnetic resonance in medicine. 2000;44(2):259-68.

93. Budde MD, Xie M, Cross AH, Song S-K. Axial diffusivity is the primary correlate of axonal injury in the experimental autoimmune encephalomyelitis spinal cord: a quantitative pixelwise analysis. The Journal of neuroscience. 2009;29(9):2805-13.

94. Farrell JA, Zhang J, Jones MV, Deboy CA, Hoffman PN, Landman BA, et al. q-space and conventional diffusion imaging of axon and myelin damage in the rat spinal cord after axotomy. Magnetic resonance in medicine : official journal of the Society of Magnetic Resonance in Medicine / Society of Magnetic Resonance in Medicine. 2010 May;63(5):1323-35.

95. Klawiter EC, Schmidt RE, Trinkaus K, Liang HF, Budde MD, Naismith RT, et al. Radial diffusivity predicts demyelination in ex vivo multiple sclerosis spinal cords. NeuroImage. 2011 Apr 15;55(4):1454-60.

96. Fox RJ, Cronin T, Lin J, Wang X, Sakaie K, Ontaneda D, et al. Measuring myelin repair and axonal loss with diffusion tensor imaging. AJNR American journal of neuroradiology. 2011 Jan;32(1):85-91.

97. Dibb R, Li W, Cofer G, Liu C. Microstructural origins of gadolinium-enhanced susceptibility contrast and anisotropy. Magnetic Resonance in Medicine. 2014.

98. Li W, Wu B, Avram AV, Liu C. Magnetic susceptibility anisotropy of human brain< i> in vivo</i> and its molecular underpinnings. NeuroImage. 2012;59(3):2088-97.

99. Liu C, Li W, Johnson GA, Wu B. High-field (9.4 T) MRI of brain dysmyelination by quantitative mapping of magnetic susceptibility. NeuroImage. 2011;56(3):930-8.

100. Rudko DA, Solovey I, Gati JS, Kremenchutzky M, Menon RS. Multiple Sclerosis: Improved Identification of Disease-relevant Changes in Gray and White Matter Using Susceptibility-based MR Imaging. Radiology. 2014.

101. Lee J, Shmueli K, Fukunaga M, van Gelderen P, Merkle H, Silva AC, et al. Sensitivity of MRI resonance frequency to the orientation of brain tissue microstructure. Proceedings of the National Academy of Sciences. 2010;107(11):5130-5.

102. Khalil M, Enzinger C, Langkammer C, Tscherner M, Wallner-Blazek M, Jehna M, et al. Quantitative assessment of brain iron by R2* relaxometry in patients with clinically isolated syndrome and relapsing–remitting multiple sclerosis. Multiple Sclerosis. 2009;15(9):1048-54.

103. Khalil M, Langkammer C, Ropele S, Petrovic K, Wallner-Blazek M, Loitfelder M, et al. Determinants of brain iron in multiple sclerosis A quantitative 3T MRI study. Neurology. 2011;77(18):1691-7.

104. McRobbie DW, Moore EA, Graves MJ, Prince MR. MRI from Picture to Proton: Cambridge University Press; 2006.

105. Matteini P, Ratto F, Rossi F, Cicchi R, Stringari C, Kapsokalyvas D, et al. Photothermally-induced disordered patterns of corneal collagen revealed by SHG imaging. Optics express. 2009;17(6):4868-78.

106. Schomberg H, Timmer J. The gridding method for image reconstruction by Fourier transformation. Medical Imaging, IEEE Transactions on. 1995;14(3):596-607.

107. Rao RA, Mehta MR, Toussaint KC. Fourier transform-second-harmonic generation imaging of biological tissues. Optics express. 2009;17(17):14534-42.

108. Chamma E, Bélisle J, Lacroix S, De Koninck Y, Côté D. Local assessment of myelin health in a multiple sclerosis mouse model using a 2D Fourier transform approach. 2013.

109. Ambekar R, Lau T-Y, Walsh M, Bhargava R, Toussaint KC. Quantifying collagen structure in breast biopsies using second-harmonic generation imaging. Biomedical optics express. 2012;3(9):2021-35.

110. Mathias JM, Tofts PS, Losseff NA. Texture analysis of spinal cord pathology in multiple sclerosis. Magnetic resonance in medicine : official journal of the Society of Magnetic Resonance in Medicine / Society of Magnetic Resonance in Medicine. 1999 Nov;42(5):929-35.

111. Haralick RM, Shanmugam K, Dinstein IH. Textural features for image classification. Systems, Man and Cybernetics, IEEE Transactions on. 1973 (6):610-21.

112. Haralick RM. Statistical and structural approaches to texture. Proceedings of the IEEE. 1979;67(5):786-804.

113. Zhang Y, Wells J, Buist R, Peeling J, Yong VW, Mitchell JR. A novel MRI texture analysis of demyelination and inflammation in relapsing-remitting experimental allergic encephalomyelitis. Medical Image Computing and Computer-Assisted Intervention–MICCAI 2006: Springer; 2006. p. 760-7.

114. Bonilha L, Kobayashi E, Castellano G, Coelho G, Tinois E, Cendes F, et al. Texture analysis of hippocampal sclerosis. Epilepsia. 2003 Dec;44(12):1546-50.

115. Bernasconi A, Antel SB, Collins DL, Bernasconi N, Olivier A, Dubeau F, et al. Texture analysis and morphological processing of magnetic resonance imaging assist detection of focal cortical dysplasia in extra-temporal partial epilepsy. Annals of neurology. 2001 Jun;49(6):770-5.

116. Antel SB, Collins DL, Bernasconi N, Andermann F, Shinghal R, Kearney RE, et al. Automated detection of focal cortical dysplasia lesions using computational models of their MRI characteristics and texture analysis. NeuroImage. 2003 Aug;19(4):1748-59.

117. Herlidou-Meme S, Constans JM, Carsin B, Olivie D, Eliat PA, Nadal-Desbarats L, et al. MRI texture analysis on texture test objects, normal brain and intracranial tumors. Magnetic resonance imaging. 2003 Nov;21(9):989-93.

118. Mahmoud-Ghoneim D, Toussaint G, Constans JM, de Certaines JD. Three dimensional texture analysis in MRI: a preliminary evaluation in gliomas. Magnetic resonance imaging. 2003 Nov;21(9):983-7.

119. Yu O, Mauss Y, Zollner G, Namer IJ, Chambron J. Distinct patterns of active and non-active plaques using texture analysis on brain NMR images in multiple sclerosis patients: preliminary results. Magnetic resonance imaging. 1999 Nov;17(9):1261-7.

120. Theocharakis P, Glotsos D, Kalatzis I, Kostopoulos S, Georgiadis P, Sifaki K, et al. Pattern recognition system for the discrimination of multiple sclerosis from cerebral microangiopathy lesions based on texture analysis of magnetic resonance images. Magnetic resonance imaging. 2009 Apr;27(3):417-22.

121. Zhang J, Tong L, Wang L, Li N. Texture analysis of multiple sclerosis: a comparative study. Magnetic resonance imaging. 2008 Oct;26(8):1160-6.

122. Loizou C, Pattichis C, Seimenis I, Eracleous E, Schizas C, Pantziaris M, editors. Quantitative analysis of brain white matter lesions in multiple sclerosis subjects: Preliminary findings. Information Technology and Applications in Biomedicine, 2008 ITAB 2008 International Conference on; 2008: IEEE.

123. Mayerhoefer ME, Breitenseher M, Amann G, Dominkus M. Are signal intensity and homogeneity useful parameters for distinguishing between benign and malignant soft tissue masses on MR images? Objective evaluation by means of texture analysis. Magnetic resonance imaging. 2008 Nov;26(9):1316-22.

124. Harrison LC, Raunio M, Holli KK, Luukkaala T, Savio S, Elovaara I, et al. MRI texture analysis in multiple sclerosis: toward a clinical analysis protocol. Academic radiology. 2010 Jun;17(6):696-707.

125. Zhang Y, Moore G, Laule C, Bjarnason TA, Kozlowski P, Traboulsee A, et al. Pathological correlates of magnetic resonance imaging texture heterogeneity in multiple sclerosis. Annals of neurology. 2013;74(1):91-9.

126. Bigun J. Vision with direction: Springer; 2006.

127. Bigun J. Optimal orientation detection of linear symmetry. 1987.

128. He B, Wu JP, Chim SM, Xu J, Kirk TB. Microstructural analysis of collagen and elastin fibres in the kangaroo articular cartilage reveals a structural divergence depending on its local mechanical environment. Osteoarthritis and cartilage / OARS, Osteoarthritis Research Society. 2013 Jan;21(1):237-45.

129. Gilbert S, Trew M, Smaill B, Radjenovic A, Bernus O. Measurement of myocardial structure: 3D structure tensor analysis of high resolution MRI quantitatively compared to DT-

MRI. Statistical Atlases and Computational Models of the Heart Imaging and Modelling Challenges: Springer; 2013. p. 207-14.

130. Budde MD, Frank JA. Examining brain microstructure using structure tensor analysis of histological sections. Neuroimage. 2012 Oct 15;63(1):1-10.

131. Sotiropoulos SN, Chen C, Dikranian K, Jbabdi S, Behrens T, Van Essen DC, et al., editors. Comparison of diffusion MRI predictions and histology in the macaque brain. Proceedings of the International Society for Magnetic Resonance in Medicine (ISMRM) Annual Meeting, Salt Lake City; 2013.

132. Lucchinetti C, Bruck W, Parisi J, Scheithauer B, Rodriguez M, Lassmann H. Heterogeneity of multiple sclerosis lesions: implications for the pathogenesis of demyelination. Annals of neurology. 2000 Jun;47(6):707-17.

133. Fonck E, Feigl GG, Fasel J, Sage D, Unser M, Rüfenacht DA, et al. Effect of aging on elastin functionality in human cerebral arteries. Stroke. 2009;40(7):2552-6.

134. Lacroix S, Hamilton LK, Vaugeois A, Beaudoin S, Breault-Dugas C, Pineau I, et al. Central canal ependymal cells proliferate extensively in response to traumatic spinal cord injury but not demyelinating lesions. PloS one. 2014;9(1):e85916.

135. Bayan C, Levitt JM, Miller E, Kaplan D, Georgakoudi I. Fully automated, quantitative, noninvasive assessment of collagen fiber content and organization in thick collagen gels. Journal of Applied Physics. 2009;105(10):102042--11.

136. Raine CS. Novel molecular mechanisms in MS. Adv Stud Med. 2004;4:S316-S21.

137. Breij EC, Brink BP, Veerhuis R, Van den Berg C, Vloet R, Yan R, et al. Homogeneity of active demyelinating lesions in established multiple sclerosis. Annals of neurology. 2008;63(1):16-25.

138. Perron JC, Dodd J. Inductive specification and axonal orientation of spinal neurons mediated by divergent bone morphogenetic protein signaling pathways. Neural development. 2011;6:36.

139. Xie J, Zhao T, Lee T, Myers E, Peng H. Anisotropic path searching for automatic neuron reconstruction. Medical image analysis. 2011 Oct;15(5):680-9.

140. Takemura SY, Bharioke A, Lu Z, Nern A, Vitaladevuni S, Rivlin PK, et al. A visual motion detection circuit suggested by Drosophila connectomics. Nature. 2013 Aug 8;500(7461):175-81.

141. Christensen PC, Brideau C, Poon KW, Döring A, Yong VW, Stys PK. High-resolution fluorescence microscopy of myelin without exogenous probes. NeuroImage. 2014;87:42-54.

142. Concha L. A macroscopic view of microstructure: Using diffusion-weighted images to infer damage, repair, and plasticity of white matter. Neuroscience. 2013.

143. Benson RR, Gattu R, Cacace AT. Left hemisphere fractional anisotropy increase in noise-induced tinnitus: A diffusion tensor imaging (DTI) study of white matter tracts in the brain. Hearing research. 2014;309:8-16.

144. Jespersen SN, Bjarkam CR, Nyengaard JR, Chakravarty MM, Hansen B, Vosegaard T, et al. Neurite density from magnetic resonance diffusion measurements at ultrahigh field: comparison with light microscopy and electron microscopy. NeuroImage. 2010;49(1):205-16.

145. Mahmoudzadeh AP, Kashou NH. Evaluation of interpolation effects on upsampling and accuracy of cost functions-based optimized automatic image registration. Journal of Biomedical Imaging. 2013;2013:16.

146. Traboulsee AL, Li D. The role of MRI in the diagnosis of multiple sclerosis. Advances in neurology. 2005;98:125-46.

147. Hou H, Andrews H. Cubic splines for image interpolation and digital filtering. Acoustics, Speech and Signal Processing, IEEE Transactions on. 1978;26(6):508-17.

148. Zitova B, Flusser J. Image registration methods: a survey. Image and vision computing. 2003;21(11):977-1000.

149. Thévenaz P, Blu T, Unser M. Image interpolation and resampling. Citeseer; 2000.

150. Miklos P, editor Image interpolation techniques. 2nd Siberian-Hungarian Joint Symposium On Intelligent Systems; 2004.

151. Varadarajan V, Krolik JL, editors. Space-time interpolation for adaptive arrays with limited training data. Acoustics, Speech, and Signal Processing, 2003 Proceedings(ICASSP'03) 2003 IEEE International Conference on; 2003: IEEE.

152. Angelini E, Henry J, Marcellino M. Interpolation and backdating with a large information set. Journal of Economic Dynamics and Control. 2006;30(12):2693-724.

153. Knuth DE. Art of Computer Programming, Volume 2: Seminumerical Algorithms, The: Addison-Wesley Professional; 2014.

154. Liu J, Yan H. Phase correlation pixel-to-pixel image co-registration based on optical flow and median shift propagation. International Journal of Remote Sensing. 2008;29(20):5943-56.

155. Rennolls K, Wang M. Enhancement of image-to-image co-registration accuracy using spectral matching methods. Warnell school of forest resources, UGA, USA. 2006.

156. Toga AW, Thompson PM. The role of image registration in brain mapping. Image and vision computing. 2001;19(1):3-24.

157. Patel V, Mistree K. A Review on Different Image Interpolation Techniques for Image Enhancement.

158. Thévenaz P, Blu T, Unser M. Interpolation revisited [medical images application]. Medical Imaging, IEEE Transactions on. 2000;19(7):739-58.

159. Keys R. Cubic convolution interpolation for digital image processing. Acoustics, Speech and Signal Processing, IEEE Transactions on. 1981;29(6):1153-60.

160. Unser M. Splines: A perfect fit for signal and image processing. Signal Processing Magazine, IEEE. 1999;16(6):22-38.

161. Singh S, Kumar V, Verma H. Reduction of blocking artifacts in JPEG compressed images. Digital Signal Processing. 2007;17(1):225-43.

162. Agarwal RP, Wong PJ. Error inequalities in polynomial interpolation and their applications: Springer; 1993.

163. Knott GD. Interpolating Cubic Splines.

164. Meijering EH, Zuiderveld KJ, Viergever MA. Image reconstruction by convolution with symmetrical piecewise nth-order polynomial kernels. Image Processing, IEEE Transactions on. 1999;8(2):192-201.

165. Hou HS, Andrews H. Cubic splines for image interpolation and digital filtering. Acoustics, Speech and Signal Processing, IEEE Transactions on. 1978;26(6):508-17.

166. Parker JA, Kenyon RV, Troxel D. Comparison of interpolating methods for image resampling. Medical Imaging, IEEE Transactions on. 1983;2(1):31-9.

167. Abdi H. The eigen-decomposition: eigenvalues and eigenvectors. Encyclopedia of measurement and statistics. 2007:304-8.

168. Lehmann TM, Gonner C, Spitzer K. Addendum: B-spline interpolation in medical image processing. Medical Imaging, IEEE Transactions on. 2001;20(7):660-5.

169. Yuan Yuana NC, Zhouac S. Adaptive B-spline Knots Selection Using Multi-Resolution Basis Set.

170. Schuff N. MRI in clinical trials. Magnetic Resonance Imaging in Movement Disorders: A Guide for Clinicians and Scientists. 2013:264.

171. Barkhof F, Filippi M, Miller DH, Scheltens P, Campi A, Polman CH, et al. Comparison of MRI criteria at first presentation to predict conversion to clinically definite multiple sclerosis. Brain : a journal of neurology. 1997;120(11):2059-69.

172. Lee MA, Smith S, Palace J, Matthews PM. Defining multiple sclerosis disease activity using MRI T2-weighted difference imaging. Brain : a journal of neurology. 1998 Nov;121 (Pt 11):2095-102.

173. Erickson B. Imaging of remyelination and neuronal health. Advances in multiple Sclerosis and Experimental Demyelinating Diseases: Springer; 2008. p. 73-92.

174. Skihar V, Silva C, Chojnacki A, Doring A, Stallcup WB, Weiss S, et al. Promoting oligodendrogenesis and myelin repair using the multiple sclerosis medication glatiramer acetate. Proceedings of the National Academy of Sciences of the United States of America. 2009 Oct 20;106(42):17992-7.

175. Lewis EB, Fox NC. Correction of differential intensity inhomogeneity in longitudinal MR images. NeuroImage. 2004 Sep;23(1):75-83.

176. Maini R, Aggarwal H. A comprehensive review of image enhancement techniques. arXiv preprint arXiv:10034053. 2010.

177. Agaian SS, Panetta K, Grigoryan AM. Transform-based image enhancement algorithms with performance measure. Image Processing, IEEE Transactions on. 2001;10(3):367-82.

178. Chaudhary C, Patil MK. REVIEW OF IMAGE ENHANCEMENT TECHNIQUES USING HISTOGRAM EQUALIZATION.

179. Chang N, Choi I, Shim H. DLS: dynamic backlight luminance scaling of liquid crystal display. Very Large Scale Integration (VLSI) Systems, IEEE Transactions on. 2004;12(8):837-46.

180. Abdullah-Al-Wadud M, Kabir MH, Dewan MAA, Chae O. A dynamic histogram equalization for image contrast enhancement. Consumer Electronics, IEEE Transactions on. 2007;53(2):593-600.

181. Kaur R, Kaur APN. A Review on Image Enhancement Techniques.

182. McCreary CR, Bjarnason TA, Skihar V, Mitchell JR, Yong VW, Dunn JF. Multiexponential T< sub> 2</sub> and magnetization transfer MRI of demyelination and remyelination in murine spinal cord. NeuroImage. 2009;45(4):1173-82.

183. Song S-K, Yoshino J, Le TQ, Lin S-J, Sun S-W, Cross AH, et al. Demyelination increases radial diffusivity in corpus callosum of mouse brain. NeuroImage. 2005;26(1):132-40.

184. Yu O, Mauss Y, Zollner G, Namer I, Chambron J. Distinct patterns of active and non-active plaques using texture analysis on brain NMR images in multiple sclerosis patients: preliminary results. Magnetic resonance imaging. 1999;17(9):1261-7.

185. Zhang Y, Zhu H, Mitchell JR, Costello F, Metz LM. T2 MRI texture analysis is a sensitive measure of tissue injury and recovery resulting from acute inflammatory lesions in multiple sclerosis. NeuroImage. 2009;47(1):107-11.

186. Ono J, Harada K, Mano T, Sakurai K, Okada S. Differentiation of dys- and demyelination using diffusional anisotropy. Pediatric neurology. 1997 Jan;16(1):63-6.